Mechanistic insights into radiopharmaceutical therapies: Spatially-resolved computational model coupling radioligand pharmacokinetics with tumour dynamics

Elahe Mollaheydar[1,2], Babak Saboury[2,3], Arman Rahmim[2,3,4], and Eric N. Cytrynbaum[5]

[1]School of Biomedical Engineering, University of British Columbia, Vancouver, BC, Canada
[2]Department of Integrative Oncology, BC Cancer Research Institute, Vancouver, BC, Canada
[3]Institute of Nuclear Medicine, Bethesda, MD, US
[4]Departments of Radiology and Physics, University of British Columbia, Vancouver, BC, Canada
[5] Department of Mathematics, University of British Columbia, Vancouver, BC, Canada

April 23, 2026

Corresponding Author: Eric N. Cytrynbaum, Email: cytryn@math.ubc.ca

Abstract

Radiopharmaceutical therapies (RPTs) offer targeted radiation delivery to tumour cells, yet treatment outcomes vary substantially across patients while dosing protocols remain largely uniform. Translating mechanistic insight into improved protocols requires models that couple radioligand (RL) pharmacokinetics, spatial tumour biology, and radiation response — a combination that existing models have not yet fully achieved. We developed a hybrid discrete-continuous model coupling a cellular automaton for spatially resolved tumour dynamics to a pharmacokinetic compartment model tracking RL from injection to tumour-cell receptor binding and internalization, linked to an energy deposition and linear-quadratic radiobiological model. Simulating treatment of heterogeneous tumours across a range of conditions, we find that treatment outcome is governed primarily by tumour size and receptor expression levels and is relatively insensitive to the injected amount. By decoupling radiobiological resistance from RL delivery effects — which are spatially correlated in real tumours but separated in our model — we show that hypoxic radioresistance alone is insufficient to prevent cure, identifying compromised RL delivery, rather than intrinsic radioresistance, as the dominant mechanism of hypoxic treatment failure. These findings provide a mechanistic basis for patient stratification by receptor expression, yield a new size-based rationale for multi-injection protocols, and demonstrate that spatially resolved modelling can reveal treatment principles inaccessible to non-spatial approaches.

Keywords: Radiopharmaceutical Therapy; Tumour Dynamics.

1 Introduction

Radiopharmaceutical therapies (RPTs) are emerging as a very promising paradigm for treating various cancers by delivering targeted radiation doses to tumour cells while sparing healthy tissues [1]. RPTs rely on the unique properties of radiopharmaceuticals, consisting of a radionuclide combined with a targeting vector, such as a peptide or antibody. These vectors selectively bind to cancer-specific markers, enabling precise delivery of cytotoxic radiation [2]. Over the past few years, RPTs have gained significant attention in the treatment of metastatic cancers, where conventional treatments may be inadequate [1, 3]. They have demonstrated great potential, specifically for neuroendocrine tumours and prostate cancer, as shown by successes with Lutetium-177 (Lu-177) [4, 5, 6] and Actinium-225 (Ac-225) [7] labeled therapies.

In RPT practice, a 'one-size-fits-all' approach to dosage and timing of injections is commonly deployed, neglecting patient-specific differences in pharmacokinetics that can produce variable delivered doses [8, 9]. The growing body of evidence supporting the efficacy of RPTs [10, 11, 12] highlights the need for a deeper understanding of the key factors that influence treatment personalization — the process of tailoring treatment to the individual characteristics of the patient and their tumour. Patient-specific factors relevant to RPT outcomes include tumour size and vascularity, receptor expression levels, and individual pharmacokinetics governing how radioligand is distributed and cleared. On the treatment design side, the adjustable parameters include the total injected activity, the number of injections and the interval between them, and the choice of radioligand and its targeting

vector. Advances in quantitative imaging and dosimetry have made it increasingly feasible to measure these patient-specific factors [13], paving the way for dosing protocols adapted to the individual. Theranostic platforms pair diagnostic imaging with therapy using the same molecular target (e.g., the PSMA protein in prostate cancer) [14, 15], offering a particularly direct route to treatment individualisation [16, 17].

Mathematical and computational models can illuminate the mechanistic basis of RPT outcomes and predict how treatment parameters — injected activity, injection timing, tumour biology — interact to determine whether treatment succeeds or fails. Among various modelling approaches, cellular automata (CA) have emerged as an effective tool for capturing spatial tumour heterogeneity at cellular resolution [18, 19, 20, 21]. A parallel tradition of compartmental PBPK models has examined how tumour-level quantities — total tumour volume, receptor expression, ligand affinity, and internalization rate — govern RL distribution and treatment outcome in ^{177}Lu-PSMA-617 therapy [22, 23, 24]. At finer spatial scales, Birindelli et al. [25] coupled histology-derived microvascular networks with a convection–reaction–diffusion model of RL transport and LQ-based cell survival to show that hypoxic, poorly vascularized regions receive subtherapeutic radiation doses in ^{177}Lu-PSMA-617 therapy, implicating RL delivery failure as a key resistance mechanism. More recently, spatially resolved models of radioligand transport in solid tumours have begun to appear [26], though coupling spatial RL delivery to tumour growth and radiation response in a unified framework remains largely unaddressed.

The radiobiological components of the present work draw on established modelling traditions: partial differential equation models of spatially distributed tumour cell populations under radiotherapy [27]; tumour control probability formulas derived from cell-cycle models distinguishing radiosensitive and radioresistant subpopulations [28]; and analyses of how repopulation kinetics within the LQ formalism inform fractionation schedule design [29]. Here, we address the gap between these traditions with a model that couples spatially resolved tumour dynamics and oxygenation with radioligand pharmacokinetics and LQ radiation response, establishing a theoretical basis for more efficient and personalized RPT protocols.

2 Methods

We developed a hybrid discrete-continuous stochastic-deterministic model to understand the effect of cancer treatment using the radiopharmaceutical ^{177}Lu-PSMA-617 on heterogeneous tumours with varying vasculature density. The full model includes a stochastic spatial CA to describe tumour growth and dynamics, a partial differential equation (PDE) for oxygen delivery, diffusion, and uptake at the cell level, a pharmacokinetic (PK) component consisting of a system of ordinary differential equations (ODEs) to track the amount of radioligand (RL) across several compartments over time, and a pharmacodynamic (PD) component describing the impact of RL on tumour cells.

The components are coupled in various ways. Tumour dynamics involve processes that depend on local oxygen (changes of state between normoxic, hypoxic, and necrotic, as well as the cell division rate) and on the radiation exposure (cell survival versus induction of apoptosis). Radiation exposure is determined by the delivery (PK), decay, and absorption (PD) of RL. The tumour cell population can also feed back onto the supply of oxygen by

occluding vessels which impacts oxygen delivery in a spatially dependent manner and total RL delivery. Below we describe the four components of the model and their coupling in more detail.

2.1 Tumour dynamics

2.1.1 Definitions and geometry

The CA consists of a two-dimensional grid of nodes which we treat as a cross section of a cube of tissue 4 mm long on each side. We use the word node to refer to the CA units instead of cells for clarity as not all nodes are biological cells (which we refer to simply as cells). Each node represents a 10 μm by 10 μm object, either a cell or the cross section of a capillary. Each simulation starts with an initial tumour seed of variable size, ranging from four cells to thousands. Cell types include normoxic, hypoxic, necrotic, and apoptotic tumour cells, and healthy cells (represented as empty nodes). Capillaries can be either open or occluded. We explicitly simulate the tumour in 2D but use a conceptual cylindrical extension into 3D for determining (i) the total number of RL receptors in the tumour and (ii) the fraction of the deposited energy that end up within the tumour. This involves counting the number of cells (P) currently in the tumour in the 2D simulation domain, determining the radius, r_{eff}, of a circle with the same area as that many cells by solving $\pi r_{\text{eff}}^2 = (100\mu m^2)\ P$, and taking the cylinder height to be $2r_{\text{eff}}$. With this geometry in mind, nodes can be thought of as columns of cells of the same type extending into the third dimension and as capillaries penetrating vertically through the tissue block. The circular assumption provides a first approximation to the shape of the tumours in the simulation; improving upon this would require a detailed spatial accounting of RL in the tumour which we do not do in the present model.

2.1.2 Node dynamics

We used the Hybrid Automaton Library (HAL) [30], a specialized Java library designed to manage node dynamics in tumour models. Nodes change between cell types based on the local oxygen pressure, with thresholds distinguishing normoxic (high oxygen), hypoxic (mid-range oxygen), and necrotic (low oxygen) states (see Table 1). Radiation can induce a transition from normoxic or hypoxic to apoptotic in accordance with the PD model component. Apoptotic and necrotic cells do not reproduce, consume oxygen at a negligible rate, and are incapable of converting to any of the other cell type even if oxygen increases locally. Apoptotic cells are removed within a few days and are replaced by healthy cells. Necrotic cells are not removed. See Fig. 1 for an illustration of node types and a legend for the colour encoding used in all figures.

2.1.3 Cell division

Each cell type consumes oxygen and undergoes division at different rates. Normoxic and hypoxic cells can reproduce stochastically into neighbouring empty nodes, replacing healthy cells. Division is checked once per day per cell and each cell is given a probability of dividing based on its type and the local oxygen partial pressure. Normoxic cells have a division probability of 1 when the local oxygen is above 8.7 kPa. The probability decreases linear

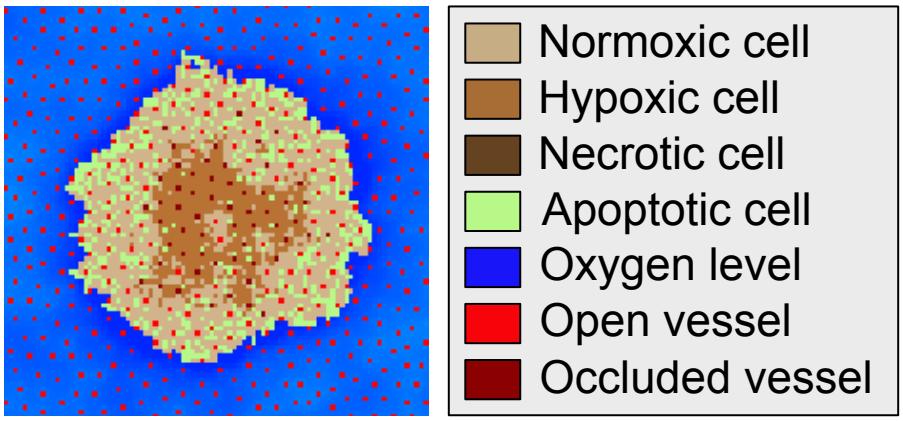

Figure 1: An illustration of the node types. The left panel is taken from a simulation and the right panel is a legend. There are no necrotic cells in the image but we include the full legend here for reference in later figures. Healthy cells are not shown explicitly and are replaced in all images of this type with the local oxygen partial pressure at that node. The oxygen field is defined at tumour and capillary nodes but not shown at those nodes here. Complete oxygen fields are included in Fig. 3.

between 8.7 kPa and 1.3 kPa with a probability of 0.15 per day at 1.3 kPa. Hypoxic cells have a probability 0.05 per day of dividing at 1.3 kPa with the rate dropping linearly to 0 at 0 kPa. Because only cells at the tumour boundary have empty neighbours available, growth is surface-driven rather than exponential, and the tumour radius increases approximately linearly in time. This growth model produces an observed growth rate of the tumour radius of around 3.5 μm/day as can be seen in Fig. 3 (essentially 0 to 500 μm in 140 days). Division rates vary continuously with local oxygen pressure, and since cell type is also determined by oxygen pressure, normoxic cells always divide faster than hypoxic cells. This bias is reinforced by the requirement of an empty node: hypoxic cells, residing deeper within the tumour, rarely have empty neighbours available for division.

As it matters for understanding the reoxygenation phenomenon described in the Results section, we make the order of steps explicit here. A cell first undergoes any changes of state (e.g. normoxic to hypoxic), then there is a check for division followed by a survival check and finally a neighbour check to see if a surviving cell that is trying to divide has a node available for it to do so. This means that a hypoxic cell is less likely to die from radiation because of radioresistance (see Section 2.4) and a slower division rate but not for the lack of a neighbouring site in which to divide.

2.2 Oxygen

2.2.1 Vasculature configuration

Capillary positions are generated by placing N capillaries uniformly at random in the 4 mm $\times$ 4 mm domain and then iteratively applying a pairwise repulsive force between capillaries closer than a cutoff radius R_{repel}, with force magnitude proportional to $(R_{\text{repel}} - d)$ and

directed along the line of centres (a rectified linear spring), where d is the distance between capillaries. Iterations were run long enough so that capillaries were a minimum distance apart but not so long that lattice patterns appeared.

Two CSV files of capillary locations were generated, one for each of two capillary densities: 605 cap/mm^2 (high density, $N = 9680$) and 420 cap/mm^2 (low density, $N = 6720$). The former was chosen to ensure that the capillaries were a few cell lengths apart and that the resulting oxygen distribution supported typical tumour division rates. The latter was chosen to create a lower oxygen background that would not induce hypoxia but was low enough to generate measurable differences in tumour dynamics (e.g. as shown in Fig.6). The CSV files were loaded at the start of each simulation. The boundary condition for the oxygen PDE was calibrated separately for each configuration as described in Section 2.2.2.

2.2.2 Oxygen influx, diffusion, and consumption

The oxygen partial pressure is tracked in the same 4 mm x 4 mm domain as the CA. We assume that oxygen enters the domain at capillaries at a rate proportional to the difference between the fixed arterial oxygen pressure u_B and the domain pressure at the capillaries' node. Consumption occurs at all non-capillary nodes at a rate determined by the cell type. Oxygen in the domain diffuses through the interstitial space. The PDE for $u(x, y, t)$, the oxygen partial pressure at location (x, y) at time t, is given by

$$u_t = D_{O_2}\nabla^2 u + c(x, y)u - pv(x, y)(u_{cap} - u)$$

where D_{O_2} is the diffusion coefficient of oxygen, $c(x, y)$ is the consumption rate, p is the permeability of the capillary walls, $v(x, y)$ the indicator function for open capillaries (zero at cells and occluded capillaries and one at open capillaries) and u_{cap} is the pressure of oxygen in the capillaries. Because the time scale of oxygen diffusion is fast compared to changes in the cell population, we treat the oxygen dynamics as being in quasi-steady state [31]. We set $u_t = 0$ and solve a discrete version of the resulting PDE using Red-Black Successive Over-Relaxation. Part of the solution to one instance of this PDE is shown in Fig. 1 (blue background) and several complete solutions are shown in the bottom row of Fig. 3. Parameters used in the oxygen submodel are reported in Table 1.

At the boundaries of the domain, we impose a non-homogeneous Dirichlet condition, setting the pressure to a fixed value. We determine this value by running a tumour-free version of the model to steady state on the capillary configuration to be used in the actual tumour simulation. We spatially average the steady-state oxygen pressure and use the resulting value as the boundary value for the tumour simulation.

We use a simple model to capture the effects of pressure-based occlusion - we count tumour cells within a 100 μm neighbourhood of the capillary and occlude it with a probability at each time step that the count exceeds a threshold (50% of the neighbourhood). Capillaries can reopen in a similar manner but with a lower local-density threshold.

2.2.3 Pre-simulation for hypoxia development

To simulate tumours with fully developed hypoxic regions, we used a pre-simulation procedure prior to the main simulation. Starting from an initial fully normoxic tumour seed, we ran the

Oxygen delivery	**Values**	**units**	Source
Oxygen diffusion	2×10^{-5}	cm^2/s	[32, 33]
Capillary oxygen pressure	13	KPa	[34]
Oxygen consumption			
Healthy cell	0.4	s^{-1}	[35]
Normoxic tumour cell	2	s^{-1}	[36]
Hypoxic tumour cell	0.8	s^{-1}	[37]
Apoptotic/necrotic cell	3×10^{-4}	s^{-1}	–
Oxygen thresholds			
Normoxic / Hypoxic transition	1.3	kPa	[38]
Hypoxic / Necrotic transition	67	Pa	[38]

Table 1: Oxygen-related parameters. The consumption rates were used to define a discrete version of the function $c(x, y)$ where each (x, y) corresponded to a single cell. The apoptotic and necrotic consumption rates were chosen to be negligible compared to the others. The normoxic-hypoxic and hypoxic-necrotic thresholds were chosen to be consistent with the ranges reported in [38] for radiobiological hypoxia and near-anoxic conditions respectively.

model for 40 days with cell division suppressed and no RL injections. During this period, capillaries surrounded by sufficient tumour cells occluded, and the oxygen field equilibrated to the resulting vascular configuration, allowing hypoxic and necrotic regions to develop. The resulting tumour was then used as the initial state for the full simulation.

2.3 Radioligand pharmacokinetics

The pharmacokinetic component of the full model consists of a compartment submodel that tracks RL concentration from injection through to internalization within tumour cells. The submodel includes a central vascular compartment into which RLs are injected, and four compartments local to the tumour: vascular, extracellular, tumour-cell bound, and intracellular. The tumour vascular compartment, which we assume is primarily capillaries and will refer to as the capillary compartment, is fed by flow from the central vascular compartment and feeds into the extracellular compartment by capillary wall permeability. From there, the RLs can bind specifically to tumour cells and can be internalized with their receptors. The radioactive isotope portion of internalized RLs can be released from a cell following autophagy of the RL. We treat release as removal from the system instead of adding an additional compartment. The compartments track total RL rather than a spatial distribution of RL, an assumption addressed in more detail in Section 2.4. We use the cylindrical extension described above to estimate the total number of receptors in the tumour and use that number in the binding rate. This component of the model is illustrated in Figure 2.

Within the PK submodel, there is a wide range of time scales. Using multiple-time-scale analysis, we derived a four-variable reduced system for the slow-changing variables N^x_{cen}, the amount of hot $(x = H)$ and cold $(x = C)$ RL in the central vascular compartment, and N^x_{ic},

the amount of hot and cold RL in the intracellular compartment. The equations are

$$\frac{dN^x_{\text{cen}}}{dt} = -\lambda_{\text{bio}} N^x_{\text{cen}} - k_{\text{int}} N^x_{\text{b}} + (-1)^{n_x} \lambda_{\text{decay}} N^H_{\text{cen}}, \tag{1}$$

$$\frac{dN^x_{\text{ic}}}{dt} = k_{\text{int}} N^x_{\text{b}} - k_{\text{rel}} N^x_{\text{ic}} + (-1)^{n_x} \lambda_{\text{decay}} N^H_{\text{ic}} \tag{2}$$

where $n_H = 1$, $n_C = 2$ (these exponents on (-1) ensure that radioactive decay moves RL out of the hot and into the cold state), and N^x_{b}, the amount of RL bound to tumour cells, is

$$N^x_{\text{b}} \approx R_T \frac{N^x_{\text{cen}}}{N_{\text{cen}} + K_M} \tag{3}$$

where $N_{\text{cen}} = N^H_{\text{cen}} + N^C_{\text{cen}}$, $R_T = PR_C$, $K_M = V_{\text{cen}}(k_{\text{off}} + k_{\text{int}})/k_{\text{on}} = 4.3$ nmol, and all other parameters are defined in Table 2. The term N_{cen}, appearing in the denominator of the Michaelis-Menten-like rate in both ODEs, illustrates the competitive inhibition of cold RL in the binding saturation of hot RL. The other variables are N^x_{cap}, the amount of RL in the capillary compartment, and N^x_{ec}, the amount of RL in the extracellular space around the tumour cells. They are in rapid equilibrium with the central vascular compartment:

$$N^x_{\text{cap}} \approx V_{\text{cap}} \frac{N^x_{\text{cen}}}{V_{\text{cen}}}, \tag{4}$$

$$N^x_{\text{ec}} \approx V_{\text{ec}} \frac{N^x_{\text{cen}}}{V_{\text{cen}}}. \tag{5}$$

The total number of cells in the tumour, P, determines the tumour volume, V (each cell is 10^3 μm^3), V_{ec} is a constant fraction of the tumour volume $V_{\text{ec}} = 0.4V$ and V_{cap} is determined by the formula $V_{\text{cap}} = n_{\text{cap}} A_{\text{cap}} h_{\text{tumour}}$ where n_{cap} is the number of capillaries within the region occupied by the tumour, A_{cap} is the capillary cross-sectional area (100 μm^2) and $h_{\text{tumour}} = 2r_{\text{eff}}$.

Eqs. (1) and (2) and the approximations (3), (4), and (5) are derived from the quasi-steady state equations of the multiple-time-scale analysis. The details of the derivation of these equations are given in the Appendix (5.1). Parameter values are given in Table 2.

2.3.1 Injection protocol

Radioligand was injected as a bolus into the central vascular compartment. Each injection consisted of a mixture of hot (radiolabeled, ^{177}Lu) and cold (unlabeled) RL in a fixed ratio of 10% hot to 90% cold by molar amount. Both hot and cold RL were capable of binding (competitively) to receptors but only the hot RL delivered radiation.

The injected amount and injection schedule varied by experiment:

- *Single-injection simulations* (Figs. 4 and 5): a single injection of 100 nmol total RL on Day 5.
- *Tumour-size sweep* (Fig. 6): a single injection of 50 nmol on Day 5. This amount was chosen to place the simulations in a regime where the fail-cure transition was clearly visible across the size range tested. It also matches the average injected amounts per injection in the interval-skew sweep (see Section 3.6).

Rate constants	**Symbol**	**Value**	**Units**	Source
^{177}Lu decay	λ_{decay}	7.1×10^{-5}	min^{-1}	[39]
Central vascular compartment clearance	λ_{bio}	1.6×10^{-4}	min^{-1}	[40]
Binding	k_{on}	1.5×10^{-3}	$\ell\ \text{nmol}^{-1}\ \text{min}^{-1}$	[41]
Unbinding	k_{off}	1.2×10^{-2}	min^{-1}	[41]
Internalization	k_{int}	0.001	min^{-1}	[25, 22, 23]
Release	k_{rel}	2×10^{-4}	min^{-1}	[25, 42]
Compartment volumes				
Central vascular	V_{cen}	0.5	ℓ	[42]
Tumour vascular	V_{cap}	$2r_{\text{eff}}n_{\text{cap}}A_{\text{cap}} \times 10^{-15}$	ℓ	–
Tumour extracellular	V_{ec}	$0.4n_{\text{cell}}V_{\text{cell}}$	ℓ	[43, 42]
Receptor-related parameters				
Receptors per tumour cell	R_C	5×10^{-10}	nmol	[44, 42]

Table 2: Definitions and values for the parameters in the PK model. The tumour vascular (or capillary) compartment volume is the tumour height ($2r_{\text{eff}}$) multiplied by the number of capillaries in the tumour (n_{cap}) multiplied by the cross-sectional area of a capillary. The 10^{-15} converts μm^2 to litres. The tumour extracellular compartment is 40% of the tumour volume which is the number of tumour cells in the 3D extension n_{cell} (all types because this is used to calculate total receptor content) multiplied by the volume of each cell ($V_{\text{cell}} = 1000\ \mu\text{m}^3$). R_C, the amount of receptors per tumour cell which we refer to as the receptor density, is varied in the receptor-density study but is as given above in all other simulations.

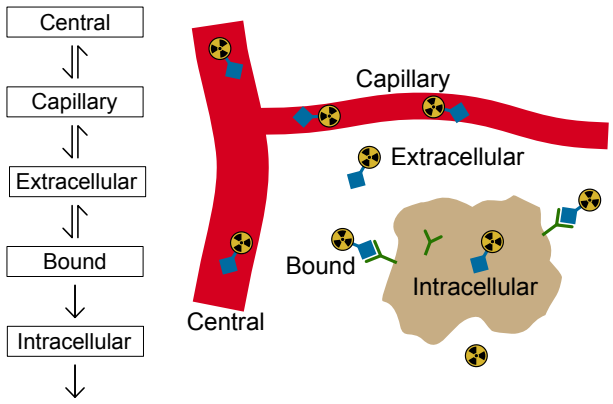

Figure 2: The compartment submodel used to track the delivery of RLs to the tumour and its distribution within the tumour tissue. It consists of five compartments as shown. RLs are injected into the blood, from which they transfer to the capillary compartment and then the extracellular space. They can bind to tumour-cell receptors, entering the bound state. Subsequently, the RLs can get internalized within tumour cells and may be subsequently released. The illustrations beside each compartment show anatomical views of the compartments for clarity but the model just tracks the total concentration of RL in each compartment.

- *Injected-amount–receptor-density sweep* (Fig. 7): a single injection on Day 5 with total injected amount varying from 12.5 to 200 nmol and receptor density varying from 3.4×10^{-10} to 8.2×10^{-10} nmol/cell across the sweep grid. The baseline receptor density used in all other simulations was $R_C = 5 \times 10^{-10}$ nmol/cell.

- *Interval-skew sweep* (Fig. 9): two injections with a total of 100 nmol. The first injection of $50 + S$ nmol is given on Day 5 and the second injection of $50 - S$ nmol is given D days later. The skew S ranges from -25 to 25 nmol and the inter-injection interval D ranges from 2 to 22 days.

We have reported the injected amounts in nmol because the RL have a biochemical role in the PK submodel in addition to its radiobiological role, for example, binding to receptors which are measured in nmol. Because we always use 10% hot fraction, the conversion is straightforward — 100 nmol is 7,268 MBq or 196 mCi. This is the most common injected amount/activity used in our studies, with 50 nmol (3634 MBq or 98 mCi) also being used and a range of 12.5 nmol through 200 nmol (908.5 MBq through 14536 MBq or 24.5 mCi through 392 mCi) being the amounts/activities used in the injected-amount–receptor-density sweep (Section 3.5).

2.4 Radioligand pharmacodynamics

When ^{177}Lu decays, the emitted beta particle can travel up to a few millimeters. The tumours in our model are in the range of 10-600 μm in diameter and the spatial domain is 4 mm across; we do not track the spatial distribution of RLs in the tumour and instead adopt a "well-mixed" assumption — a reasonable approximation given the mm-scale beta-emission range for ultimate dose calculations. We calculate the total amount of hot RL in the tumour and convert that into a dose rate

$$D'(t) = \frac{\bar{E}_\beta^{177\mathrm{Lu}} N_A \lambda_{\mathrm{decay}} N_{\mathrm{tot}}^{\mathrm{hot}}(t) f_{\mathrm{deposit}}(t)}{m_{\mathrm{tumour}}(t)}$$

where $\bar{E}_\beta^{177\mathrm{Lu}}$ is the average energy of a beta particle, N_A is Avogadro's number, λ_{decay} is the radioactive decay rate, $N_{\mathrm{tot}}^{\mathrm{hot}}$ is the total amount of hot RL in the tumour compartments in mol, f_{deposit} is the fraction of radiation deposited in the tumour (see Section 2.4.1 below), and m_{tumour} is the current mass of the tumour.

2.4.1 Energy deposition fraction

When RLs concentrated within the tumour decay, the energy is deposited at a distance according to a dose point kernel (DPK). By integrating the DPK against a spatial distribution of RL, we can calculate the dose delivered at any point in space in or around the tumour. Some energy will be deposited outside the tumour and this loss of energy is worse for smaller tumours, ultimately going to zero as the tumour radius goes to zero. We refer to the fraction of the total energy deposited that lands within the tumour the intratumoural energy deposition fraction (EDF). In all the simulations presented here, we used a DPK derived from a Monte Carlo (MC) simulation (reported elsewhere) to calculate what fraction (f_{deposit}) of the energy

Coefficient	Value	Units	Source
α_{norm}	0.15	Gy^{-1}	[48, 49]
β_{norm}	0.05	Gy^{-2}	[48, 49]
α_{hypo}	0.1	Gy^{-1}	[50, 51]
β_{hypo}	0.02	Gy^{-2}	[50, 51]

Table 3: Coefficients for the survival probabilities.

emitted from RL within the tumour is deposited within the tumour [45]. Because we track total RL in each compartment and not the spatial distributions, we assume that the tumour is spherical with RL distributed uniformly across the sphere. Values of f_{deposit} are calculated in advance for a set of radii which we use as a lookup table for interpolation on the fly.

Because we relied on unpublished results (the MC simulation), we also used an alternative method to estimate f_{deposit} for clarity of explanation and to show qualitative agreement with a simplified approach. In place of the MC DPK, we also used a DPK consisting of a constant value on the interior of a sphere of radius ℓ and zero outside the sphere. Because the DPK represents redistribution without loss, the constant value is chosen so that the integral of the DPK over all of space is one. Because the volume of the intersection of two spheres has an explicit formula (found by integrating a surface of revolution), the calculations are exact. We found the value of ℓ that gave the best fit of this "uniform-sphere redistribution" DPK model to the MC DPK model. The behaviour of the model using the uniform-sphere redistribution DPK model is qualitatively the same as for the MC DPK model. Details of the uniform sphere DPK model and the best fit to the MC DPK model are given in Appendix 5.3.

2.4.2 Survival probability

Throughout a simulation, we keep track of an average state of DNA damage in tumour cells, by age cohort, using a system of ODEs for accumulated dose (D), single-strand damage (A), and double-strand damage (G_{alt}). See Appendix 5.4 for details. When a cell attempts to divide, it has a survival probability (more specifically a probability of having unrepaired lethal DNA damage) that is determined by the ODE states:

$$SF = \exp\left(-\alpha D - 2\beta G_{\text{alt}}\right).$$

This is a slightly reformulated version (equivalent to the standard formulation) of the Linear-Quadratic (LQ) model with the Lea-Catcheside correction factor [46, 47] to account for ongoing cellular repair. Sensitivity to radiation is modeled by allowing α and β to depend on cell type, with hypoxic cells more resistant to radiation than normoxic cells. Parameter values are given in Table 3.

3 Results

3.1 Tumour growth in the absence of treatment

We simulated a growing tumour without RL injection to illustrate and characterize the tumour dynamics submodel. Four snapshots of a growing tumour are shown in the top row of

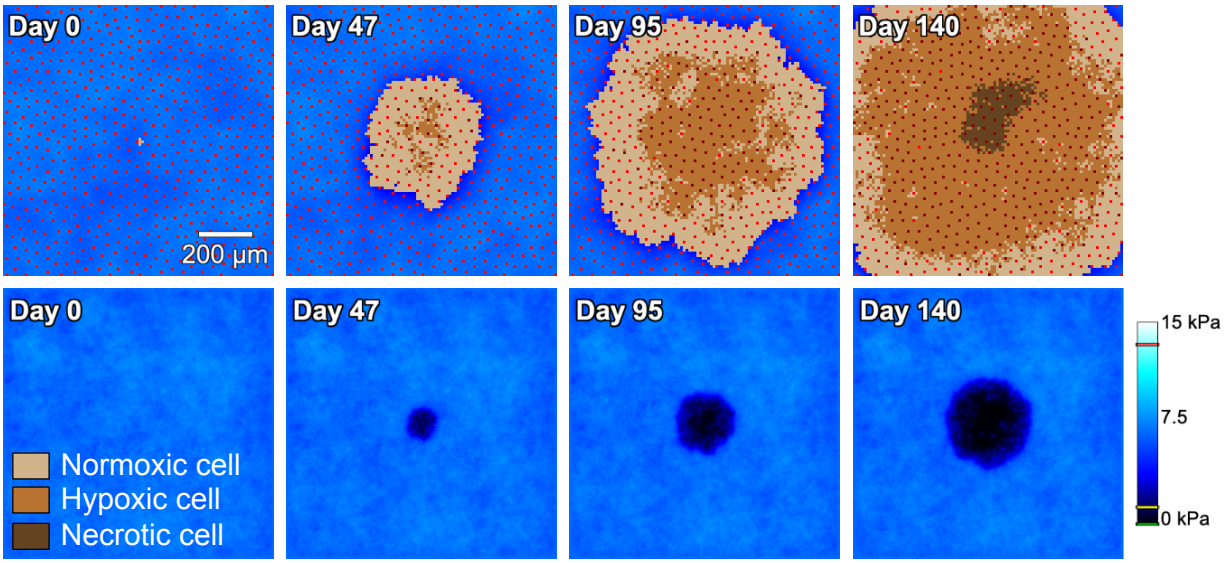

Figure 3: Tumour growth without treatment. Starting with a small and fully normoxic (light brown) tumour consisting of four cells, hypoxic regions (darker brown) begin to appear and eventually necrotic patches (darkest brown). The tumour is shown over the oxygen field in the top row and the oxygen field alone in the bottom row. The tumour images are magnified by a factor of four for clarity, showing a 1mm x 1mm region around the tumour. The oxygen-only images shows the full 4mm x 4mm domain. The colour bar on the right shows oxygen partial pressures. Important oxygen levels are marked by coloured lines across the scale bar: capillary oxygen (red), the hypoxic threshold (yellow), the necrotic threshold (green).

Fig. 3. The initial tumour consisted of four normoxic cells. Over 120 days, it grew to about 1 mm in diameter (over 10,000 cells), during which time numerous capillaries (red) on the interior were occluded (dark red) leading to the appearance of a large hypoxic region and a smaller necrotic core (see legend for colours). In the lower row of Fig. 3, the tumour was omitted from the image providing a view of the complete oxygen field. Barely visible bright spots indicate the presence of open capillaries (red in the upper images). Capillaries were spread uniformly throughout the domain with a typical spacing of 3–5 cell lengths so the regions under the tumour lacking blue spots contain hundreds of occluded capillaries and line up with the hypoxic and necrotic regions shown in the top row. The magnification in the upper panels is 4x that in the lower panels so, even though it does not appear so, the tumours actually fit into the dark patches.

3.2 Tumour size determines the energy deposition fraction and treatment outcome

We simulated three tumours of different sizes, illustrated in Fig. 4. Conditions, aside from initial size, were the same in all three simulations but responses to treatment differed.

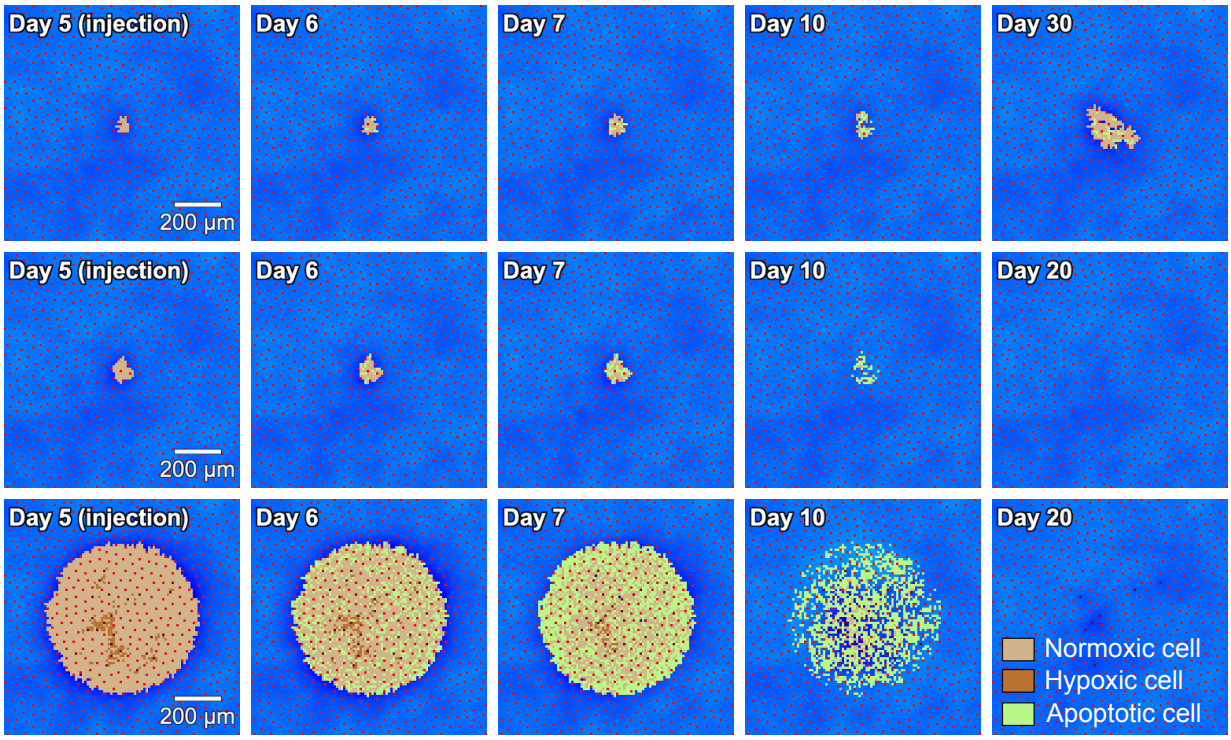

Figure 4: Three growing tumours of different sizes but otherwise the same conditions under RPT treatment with minimal hypoxia present (in the large tumour only). Top row: Treatment of a small tumour (initially eight cells) failed. Middle row: An intermediate-sized tumour (initially 28 cells) was just above the size threshold of treatment success upon injection for the given conditions. Bottom row: For the largest tumour tested (600 μm diameter, ~ 2650 cells), treatment was successful and displayed a similar time-course to the intermediate-sized tumour, with the tumour eliminated by Day 20. As described in the text, these differing responses can be explained by the energy deposition fraction.

Treatment failed for the smallest tumour (initially eight cells) due to the survival of some cells that continued to grow after treatment. The intermediate- (initially 28 cells) and large-sized tumours (initial diameter 600 μm or roughly 3000 cells) responded well, being eliminated by day 30. Although the injected amount was the same for all three, the energy deposition factor f_{deposit} modulated the dose significantly — the vast majority of beta particles emitted from the small tumor were deposited outside the tumor. The factors for the three tumours were $f_{\text{deposit}}^{\text{small}} = 1.2\%$, $f_{\text{deposit}}^{\text{intermediate}} = 10\%$, and $f_{\text{deposit}}^{\text{large}} = 59\%$, introducing a large difference in effective doses between the smallest and larger tumours.

The two smaller tumours were too small for hypoxia to be a factor. For the large tumour, we set the cells to be normoxic at the start and, with only five days before treatment, only about 60 out of 3000 were hypoxic by that time. In the next section, we report on treatment results for a tumour of the same size with fully established hypoxia.

3.3 Hypoxic resistance

The tumours tested and shown in Fig. 4 were all well-oxygenated at the time of treatment. For the largest tumour, this was an artifact of the initial conditions of the simulation. These normoxic tumours illustrate the impact of the loss of energy due to deposition outside the tumour. A more realistic tumour would include hypoxic cells which are resistant to radiation. A larger tumour, in reality and in the model, would have a larger fraction of hypoxic cells due to the occlusion of capillaries under tumour-induced pressure and limits on the diffusion of oxygen. Hypoxic resistance to radiation treatment could reverse the trend observed in Fig. 4.

To test whether hypoxic resistance would reverse this trend, we simulated tumours of the same sizes, this time running the pre-simulation stage described in Section 2.3.1 to establish fully developed hypoxia before running the full simulation.

The smallest and intermediate tumours were too small to develop hypoxia and so the results for these two were exactly the same as shown in Fig. 4. Over the 40 days of pre-simulation, about 43% of the cells in the large tumour became hypoxic. Fig. 5 shows that tumour being eliminated by the treatment, indicating that hypoxia was insufficient to protect it. Examining the images, we see that the majority of the initial thin outer shell of normoxic cells and the scattered normoxic cells on the interior turned apoptotic within a couple days of the injection. The subsequent images give the appearance of the tumour undergoing an erosive process from the outside inward. The entire tumour is eliminated by Day 40.

Hypoxic cells are both less radiosensitive and divide much less frequently than normoxic cells (at most a 0.05 probability each day) suggesting that this erosion process was driven by reoxygenation of hypoxic cells thereby reverting them to normoxic and increasing their radiosensitivity and division rate. We extended the apoptotic removal time to test whether keeping tumour cells present longer, thereby maintaining capillary occlusion longer, would lead to tumour survival or at least extend its presence. Even with apoptotic cells staying around ten times longer (20 day average removal time), treatment still succeeded and the time to elimination was essentially the same despite the prolonged presence of apoptotic cells. Examination of the simulation output revealed that capillaries did not reopen, as expected, but the drop in oxygen consumption with the change of normoxic cells to apoptotic was sufficient to trigger the inward wave of reoxynation.

3.4 Tumour-size dependence

The simulations in Fig. 4 suggested that tumour size is a key determinant of treatment success. To quantify this more rigorously, we swept over initial tumour size with 150 replicates per size, using an injection amount of 50 nmol, and recorded the cure rate. This injection amount was chosen to best illustrate the fail/cure transition and for consistency with the two-injection protocol described later. We also repeated the sweep at a lower capillary density (420 vs 605 cap/mm^2) to test the effect of a clinically relevant source of inter-patient variability. Since the hypoxic tumour in Fig. 5 was eliminated despite hypoxic resistance, we also measured time to elimination to quantify what effect that resistance does have. Results are shown in Fig. 6.

We also ran the sweep with a 100 nmol injection and found a cure threshold between 25 and 28 initial cells (not shown), consistent with the tumour size threshold suggested by Fig. 4.

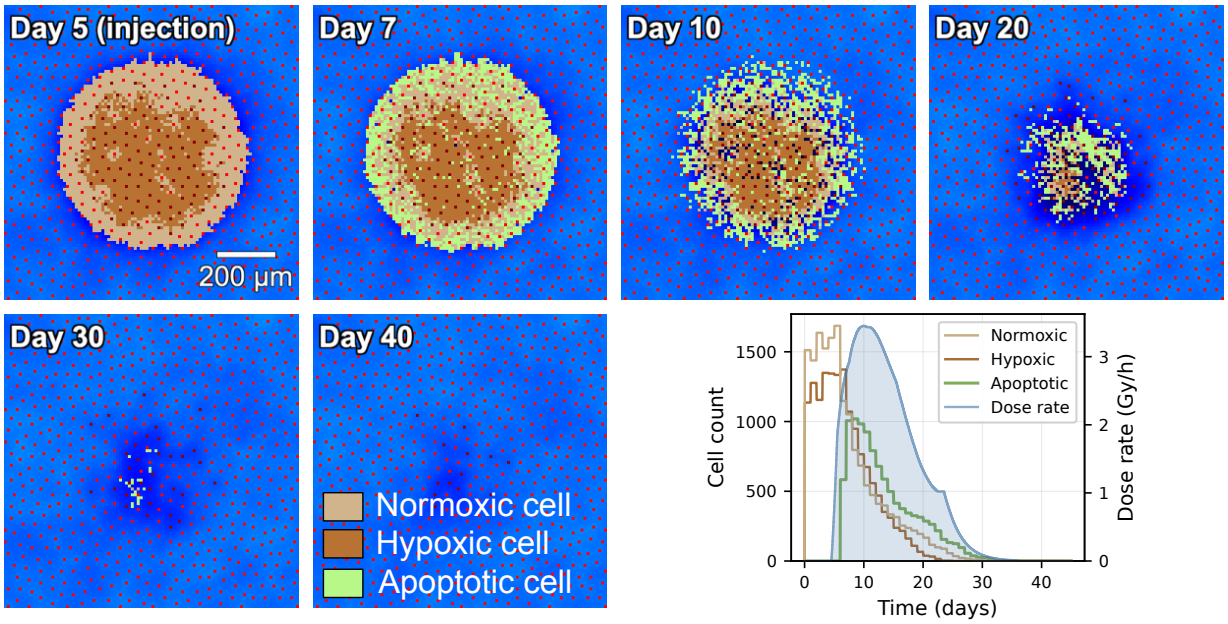

Figure 5: Treatment of a large tumour (initially 600 μm in diameter) with fully developed hypoxic regions. The presence of hypoxic regions did not have the anticipated protective effect on the final outcome despite hypoxic cells being more resistant to treatment. However, the time until the tumour was fully eliminated was significantly longer (40 days) than for the normoxic equivalent (20 days). In contrast to the normoxic tumours, which showed rapid uniform apoptosis, here an outer shell of normoxic cells went apoptotic and were subsequently removed, triggering an inward wave of erosion that progressively eliminated the tumour from the outside in. The plot shows tumour cell types population sizes and the dose rate.

Interestingly, the threshold size at injection was 50 cells, similar to the 50 nmol injection results reported below, a finding most likely explained by the saturation effect explored in Section 3.5.

The cure-rate curves for the two capillary densities are nearly identical across the full size range tested (20 to 1400 cell upon injection on day 5), with a transition from failure to success centred around 50 cells and spanning roughly 30 to 70 cells. Treatment success is therefore essentially independent of capillary density and hence of the ambient oxygenation level, at least across the range tested.

Below approximately 400–450 cells, tumours showed negligible vessel occlusion and hypoxia for both capillary densities, so both curves reflect purely normoxic biology in this range. Above 450 cells, hypoxia and associated radioresistance were present but did not cause treatment failure, consistent with Fig. 5. In the Discussion, we address how incorporating spatially resolved RL delivery — including compromised delivery due to vessel occlusion — can introduce treatment failure at larger sizes [25]. Interestingly, our uniform RL treatment decouples hypoxia-induced radioresistance from compromised RL delivery, two effects that are spatially correlated in reality and therefore difficult to distinguish clinically. This was a serendipitous side effect of a simplification introduced for computational efficiency.

The elimination-time curves in Fig. 6 reveal a more subtle story. Both show a clear minimum around 150 cells, reflecting two competing effects. At tumour sizes below the minimum, the effective dose decreases due to the EDF and the survival fraction per division attempt rises. Any cell that survives a division attempt, a more likely event at these lower sizes, is replaced by two daughter cells with no accumulated damage, which must themselves sustain damage if the tumour is to be eliminated. This can only occur while RL remains in the system, creating a limited window of opportunity to eliminate these successive generations. Thus a cure takes longer because of additional generations and is possible only within the window of time that the RL is present — a few days to accumulate and a few days of clearance and decay, consistent with the maximum of $\sim$10 days seen at the left end of the elimination-time curve. As tumour size decreases further, lower dose rates mean cells have a higher chance of dividing, pushing the opportunities for division attempts beyond the RL window, and the cure rate falls toward zero.

At large tumour sizes, hypoxic cells are present and the erosion process must cycle through successive iterations of reoxygenation, division, and apoptosis from the tumour boundary to the centre. Elimination time therefore increases with tumour radius in this regime, as seen in Fig. 6. The elimination-time curve is higher for lower capillary density most likely because of slowed cell cycle, and therefore less frequent survival checks, at lower oxygen levels.

The curve for the 605 cap/mm^2 case extends to smaller tumour sizes than the 420 curve because higher ambient oxygen supports faster pre-injection growth, producing larger tumours by Day 5 even from the same initial radius. Both curves omit data points where fewer than three cured runs were available, which is why the elimination-time plots begin at larger sizes than the cure-rate plots.

3.5 Parameter sweep varying injected amount and receptor density

Having established that tumour size is an important determinant of treatment success, we asked to what extent this is a reflection of the size dependence of the EDF or the total receptor

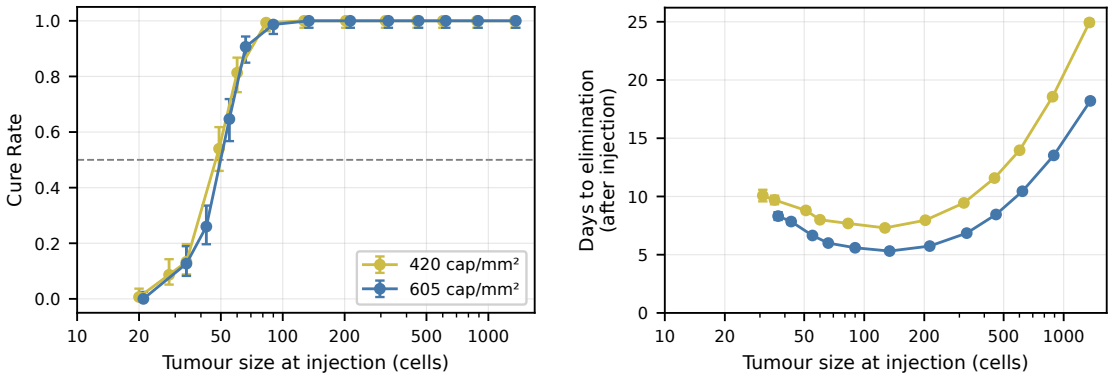

Figure 6: Treatment outcome as a function of tumour size at injection for two capillary densities (420 and 605 cap/mm^2). Left panel: Cure rate vs tumour size at injection. The two curves are statistically indistinguishable (with $n = 150$ per radius), demonstrating that capillary density has negligible effect on whether treatment succeeds. Error bars show Wilson's 95% confidence intervals. Right panel: Mean time to tumour elimination (cured runs only) vs tumour size at last injection, with error bars showing $\pm$ SEM (with $n = 150$, the error bars are only visible at the smallest tumour sizes). Lower capillary density is associated with consistently longer elimination times. Data points are omitted where fewer than three cured runs were available, resulting in the elimination-time curves beginning at larger tumour sizes than the cure-rate curves.

content of the tumour and whether increasing the injected amount could compensate for low receptor density. We simulated treatment of a small tumour (initially 11 cells) over a range of injection amounts and receptor densities. Fig. 7 shows the success rates for each parameter combination by averaging the outcome (failure $\to 0$, success $\to 1$) over 40 replicates. There is a transition zone between treatment failure and success identifiable as a noisy gray band that sweeps through the middle of the plot. For injected amounts on the right side of the plot, say above 50 nmol, the colour gradient in the horizontal direction is fairly flat but with a clear transition from low to high cure rate in the vertical direction. This suggests that treatment depends heavily on a patient's receptor density, at least through the transition, with limited scope for changing the outcome by increasing the injected amount once above 50 nmol.

Both observations can be understood through analysis of the reduced PK submodel, Eqs. (1), (2), and (3). In Appendix 5.5, we derive the following equation as an approximation of the amount of RL directly associated with the tumour (the sum of bound and internalized hot RL), what we refer to as $N^H_{\text{captive}}(t)$:

$$N^H_{\text{captive}}(t) = N^H_{\text{b}}(t) + N^H_{\text{ic}}(t) \approx \left(\frac{k_{\text{int}}}{k_{\text{rel}} + \lambda_{\text{decay}}} + 1\right) R_T \cdot \frac{0.1\, A\, e^{-(\lambda_{\text{bio}}+\lambda_{\text{decay}})t}}{A\, e^{-\lambda_{\text{bio}} t} + K_M} \tag{6}$$

where A is the injected amount, $R_T = PR_C$ is the total tumour receptor content, and $K_M = V_{\text{cen}}(k_{\text{off}} + k_{\text{int}})/k_{\text{on}}$. This approximation to $N^H_{\text{captive}}(t)$ is monotone decreasing in time (for a fixed tumour size) and so evaluating it at $t = 0$ gives a reasonable value for gauging the effectiveness of treatment. To find the relationship between R_C and A at which the cure rate is 50%, we solve

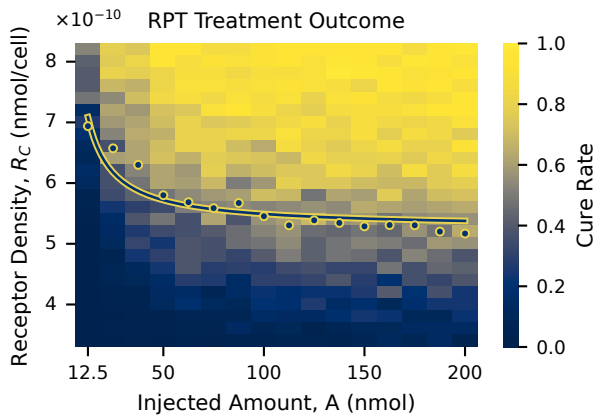

Figure 7: Cure rates for a parameter sweep through injected amounts and receptor densities. Treatment success is weakly dependent on total injected amount and strongly dependent on receptor density. The gray dashed curve with white outline is a fit of the PK submodel analysis that predicts the locus of a 50% cure rate — only one fitting parameter was required. Each rectangle represents 20 replicates, simulating treatment of a tumour consisting of 11 cells initially and 52 cells upon injection five days later. The simulation shown in the middle row of Fig. 4 appears in this parameter sweep as one of the five replicates in which the tumour was successfully treated (100 nmol injected, 5.0 $\times 10^{-10}$ nmol/cell). The horizontal axis values in equivalent mCi are 24.5 mCi, 98 mCi, 196 mCi, 294 mCi, and 392 mCi.

$$N^H_{\text{captive}}(0) \approx \left(\frac{k_{\text{int}}}{k_{\text{rel}} + \lambda_{\text{decay}}} + 1\right) P_0 R_C \cdot \frac{0.1\,A}{A + K_M} = N_{\frac{1}{2}} \tag{7}$$

where $N_{\frac{1}{2}}$ is the (unknown) captive amount that ensures a 50% cure rate and P_0 is the tumour size upon injection. This gives us

$$R_C = \sigma\left(1 + \frac{K_M}{A}\right) \quad \text{where } \sigma = \frac{N_{\frac{1}{2}}}{0.1 P_0}\left(\frac{k_{\text{int}}}{k_{\text{rel}} + \lambda_{\text{decay}}} + 1\right)^{-1}. \tag{8}$$

Using the parameter values in Table 2, we can calculate that $K_M = 4.3$ nmol. This, as a value that A can take on, lies just below the lower end of the injected amount range explored in Fig. 7 (12.5–200 nmol). This value of K_M suggests that, for values of A over 50 nmol (more than 10 times K_M), the 50% cure-rate level curve is essentially horizontal. In fact, this is still true if we replace $N_{\frac{1}{2}}$ with any value, indicating that above 50 nmol all cure-rate level curves are nearly horizontal — that is, cure rate is essentially independent of the injected amount. For values of A below 50 nmol, the cure rates eventually drop to zero as $A \to 0$ — a drop that happens more slowly around $R_C = 6 \times 10^{-10}$ nmol/cell and more abruptly for higher values of R_C.

Continuing to fill values into Eq. (8), the expression in parentheses in σ evaluates to 4.7. We also know $P_0 = 52$ cells. We are left with a single unknown parameter, $N_{\frac{1}{2}}$, or equivalently σ, with which to fit Eq. (8) to the data shown in Fig. 7. For each value of A, we fit a logistic function to estimate the 50% cure rate for that slice of the data. These points

$\left(A_i, R_C^{(i)}\right)$, shown as black dots with a yellow outline in Fig. 7, are a discrete approximation of the 50% cure-rate level curve. We fit these points using σ as the fitting parameter. Details are given in Appendix 5.6; the fitted value is $\sigma = 5.24 \times 10^{-10}$ nmol/cell and corresponding $N_{\frac{1}{2}} = 1.28 \times 10^{-8}$ nmol. The best fit $R_C(A)$ function is plotted in Fig. 7 as a black line outlined in yellow. The fitted curve lines up well with the noisy gray band — slightly below the data for $A < 100$ nmol and above it for $A \geq 100$ nmol. The value of $\sigma = 5.24 \times 10^{-10}$ nmol/cell is the horizontal asymptote of the black and yellow fitted curve. Below that value, there is low probability of treatment succeeding for any injected amount.

Further interpreting the fit, all simulations above 50 nmol are in the saturating regime where N^H_{captive} is essentially independent of A, explaining the weak observed dependence on injected radioactivity. The stronger dependence on R_C can also be understood from the fact that the R_C direction cuts directly across the level curves; thus the cure-rate surface over the R_C-A plane is steepest in the vertical direction for $A > 50$ nmol.

The fit also provides a mechanistic picture at the receptor level. At the 50% cure boundary with a typical clinical injected amount $A = 100$ nmol, approximately 96% of receptors are occupied — predominantly by cold RL, with only ∼1% occupied by hot RL. The internalized hot RL, N^H_{ic}, exceeds the bound hot RL, N^H_{b}, by a factor of $k_{\text{int}}/(k_{\text{rel}} + \lambda_{\text{decay}}) \approx 3.7$, so N^H_{ic} constitutes approximately 79% of N^H_{captive}. Since receptors are nearly saturated, additional RL has few available binding sites, whereas increasing R_C directly increases the number of available sites and thus the total captive RL.

Although this fit provides a compelling argument that the saturation of captive RL explains the insensitivity to the injected amount for clinically relevant amounts, the derivation of the fitting curve requires a few rough approximations so we also appeal directly to the pharmacokinetic data from the simulations to confirm the explanation of both dependencies. Fig. 8 shows the time course of $N^H_{\text{captive}}(t)$ from several of the simulations used to generate the image in Fig. 7. We use three values of receptor density, $R_C = 4 \times 10^{-10}$, 6×10^{-10}, and 8×10^{-10} nmol/cell, in blue, green, and red respectively. Each blue, green, and red curve shows the average of $N^H_{\text{captive}}(t)$ over 40 replicates for a single value of the injected amount. There are 13 curves of each colour corresponding to injected amounts varying from 50 to 200 nmol in increments of 12.5 nmol, each corresponding to a coloured rectangle in one of the three horizontal slices in Fig. 7. The peak value for each set of R_C curves is denoted by a dashed horizontal line of the appropriate colour.

Consistent with the analytical prediction that, above 50 nmol, we are in a saturating regime with regard to the injected amount, there is little difference among curves of the same colour despite a four-fold change in the injected amount. Also consistent with the analytical prediction is a roughly linear dependence on R_C as seen by the near doubling of the peak $N^H_{\text{captive}}(t)$ value ($0.73 \to 1.37$) corresponding to a doubling of R_C ($4 \to 8$).

3.6 Multi-injection treatment protocols

Single-injection protocols are a useful theoretical baseline, but clinical RPT typically involves multiple injections. We therefore explored how splitting the total injected amount across two injections affects treatment outcome, varying both the time between injections and the relative amounts delivered at each.

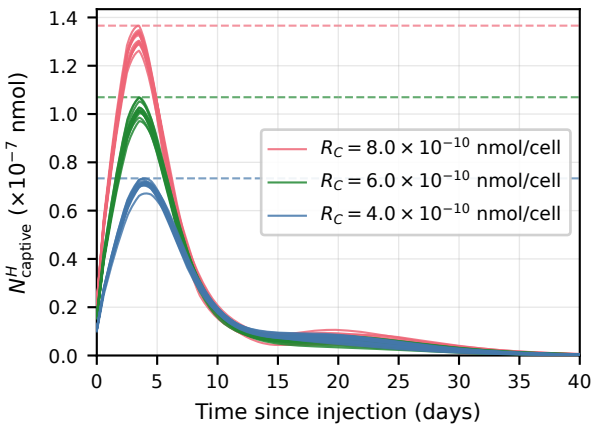

Figure 8: The parameter dependence of cure rate interpreted in terms of RL saturation. Varying the injected amount from 50 to 200 nmol (curves of the same colour) results in relatively small changes in the amplitude of N^H_{captive} while varying the receptor density (curves of different colors) produces larger changes.

Fig. 9 shows the success/failure results of treatments as a function of the inter-injection interval, D, and injection skew S, with a base injected amount I. Injections were given twice separated by D days where the first amount injected was $I + S$ and the amount injected for the second injection was $I - S$. The base amount was $I = 50$ nmol for a total injected amount of 100 nmol as in the previous parameter sweep. We varied the inter-injection interval from 2 to 22 days and the skew from -25 to 25 nmol. We use the word skew here in the sense of shifting part of a distribution from one side of the mean to the other.

As seen in Fig. 9, treatment tends to fail at low inter-injection intervals and succeed at higher intervals with only a slight dependence on the skew. We attribute both of these features to the size-dependence described in Figs. 4 and 6 — if the second injection comes too early, the tumour is still small, the energy deposition fraction is low, and treatment fails. This is reiterated by the fact that positive skew (larger first injection) is associated with slightly lower success rates (the fail-cure boundary tilts a bit to the right). For positive skews, more of the RL is injected while the tumour is smaller and is thus wasted.

To show that the dependence on inter-injection interval was due to tumour size, we extracted from the interval-skew-sweep data the tumour size at the moment of the last injection (the first injection in cases where that was sufficient to eliminate the tumour and the second injection otherwise) from every simulation with skews from -15 to 15. For each simulation, we noted the tumour size and the success of the treatment. We then binned the tumour sizes, calculated the cure rate for each bin, and plotted the results (see Fig. 10, red curve). We also replotted the curve from Fig. 6 (605 cap/mm^2) which was a direct assessment of cure rate as a function of tumour size (blue) with an injected amount of 50 nmol.

Including different skews in this calculation provided a larger number of "replicates" but introduced the possibility of increasing the variance because of different success rates associated with different injected amounts. However, the low sensitivity to injected amount seen in Fig. 7 suggested this would have minimal impact, a fact borne out by the relatively low variances compared with using only $S = 0$ (not shown).

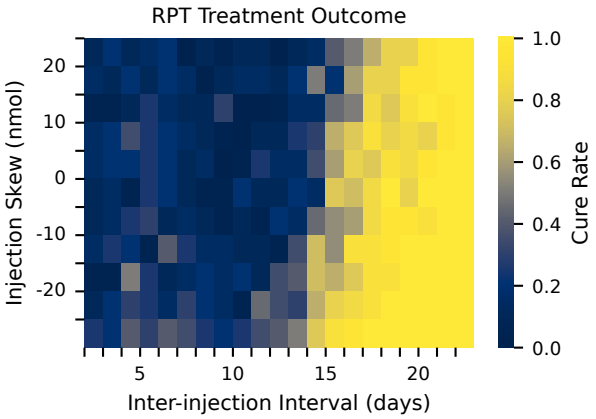

Figure 9: A parameter sweep varying the time between injections in a two-injection protocol and the skew of the injection amplitudes. All treatment simulations included a first injection on Day 5 and a second injection D days later. The first amount injected was 50 nmol + S and the second injection was 50 nmol - S where S is the injection skew. Each rectangle represents 20 replicates. Tumours consisted of four cells initially and 29 cells upon first injection five days later.

Although the failure-to-cure transitions do not occur at the same sizes (∼50 cells compared to ∼70 cells) and the baseline cure rate at low tumour sizes is elevated in the parameter sweep data (likely due to different exposure histories), both curves show a clear and relatively sharp dependence on tumour size.

4 Discussion

The results presented here tell a story organized around a single variable: tumour size at the time of injection. Tumour size determines the energy deposition fraction, governing how much of the emitted radiation is absorbed within the tumour rather than lost to surrounding tissue. Tumour size also determines the total receptor content, governing how much radioligand the tumour can capture and internalize. Both effects work in favour of treatment and increase monotonically with tumour size, producing a sharp threshold below which RPT generally fails and above which it generally succeeds. Working against treatment success, larger tumours develop hypoxic cores whose radioresistant cells might be expected to survive treatment and seed regrowth — but in the model this is largely circumvented by reoxygenation, which operates continuously through the protracted action of RPT, even without multiple injections. A more consequential size-dependent obstacle, not captured by the present model, is that the occluded capillaries in larger tumours that cause hypoxia also restrict RL delivery in exactly the regions where radioresistance is highest. Understanding these competing size dependencies — and the conditions under which the beneficial ones dominate — is central to the mechanistic picture developed here.

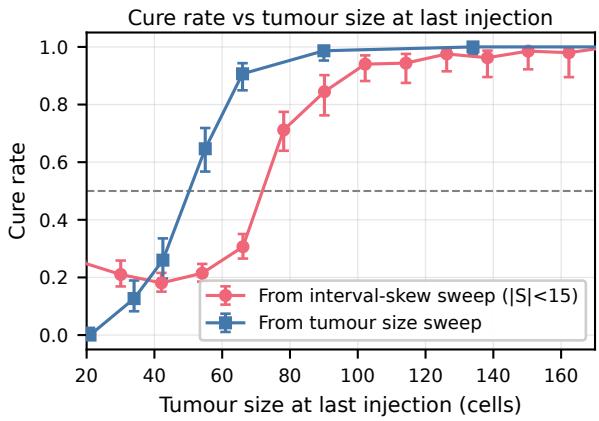

Figure 10: Cure rate as a function of tumour size at the time of last injection. Blue squares: Cure rates are taken from the tumour-size sweep, in which tumours of varying initial size were each treated with a single 50 nmol injection (same curve as in the left panel of Fig. 6). Red circles: Tumour sizes at the time of the last injection were extracted from the interval-skew sweep data (Fig. 9) and binned. The cure rate for each bin was calculated and cure rate was plotted against binned tumour size. Skews with $|S| \leq 15$ nmol were included (see main text for details). Error bars show Wilson 95% confidence intervals. Both curves show a sharp transition from low to high. The elevated baseline cure rate on the red curve (< 70 cells) probably reflects accumulated damage from a first injection.

4.1 General size dependence

The model predicts that, for the specific parameter values explored in our simulations, tumours above the threshold of roughly 50 cells ($\sim$40 μm radius) should be eliminated by RPT — a size far below the current detection limit of clinical PET imaging, which is approximately 5–15 mm in diameter depending on lesion contrast and scan time [52, 53]. This suggests that RPT may be particularly effective against micrometastases that are too small to detect or target with other modalities. Because of their narrower DPK, alpha-emitting radiopharmaceuticals have EDFs that drop to zero at even lower tumour radii, suggesting that they would be effective at eliminating even smaller tumours.

4.2 Receptor density as a lever for improving outcomes

As shown in Fig. 7 and explained via the quasi-steady-state analysis in Section 3.5, treatment outcome depends strongly on receptor density and only weakly on injected amount, at least for amounts in the parameter regime explored in the model. The strong dependence on R_C is made evident in Eq. (7) where it appears as a linear factor in N^H_{captive}. The weak dependence on the injected amount is explained by receptor saturation at $K_M \approx 4.3$ nmol. The broader implication is that receptor density is a more productive lever for improving outcomes than escalating the injected amount. Modulating the injected radioactivity is a relatively straightforward option in therapy, and can improve therapy for some tumors of different expression levels [24]. Nonetheless, the observation in this study that modulating

receptor content (expression) can have higher impact should be explored further. Although receptor density is not currently a tunable treatment parameter in clinical RPT, patient stratification by receptor expression could be a viable strategy. Tumour-cell specific receptor upregulation, if achievable, could be a worthwhile avenue of research to exploit the sensitivity reported here.

In fact, a related paradigm is already well-known in radioiodine therapy of thyroid cancer, where "redifferentiation" strategies are used to restore expression of the sodium–iodide symporter (NIS) and thereby re-enable radioiodine uptake [54]. In particular, inhibition of the MAPK pathway with BRAF or MEK inhibitors (e.g., Dabrafenib or Trametinib) has been shown to increase iodine avidity in previously refractory disease. Analogous strategies are on the horizon for PSMA RPTs, such as androgen receptor pathway inhibition, and more broadly genetic and epigenetic regulation of receptor expression, offering promising avenues to enhance radioligand uptake and therapeutic efficacy [55]. Future studies should aim to better characterize and leverage receptor upregulation as a means to improve outcomes in radiopharmaceutical therapy.

The saturation argument, as a tool for understanding the weak dependence on the injected amount, applies most appropriately at the time of injection. As the tumour responds to treatment, R_T changes with tumour size, and the usefulness of the N^H_{captive} approximation is undermined. However, the conclusion is robust: if treatment succeeds, R_T falls and captive RL falls with it; if treatment fails, R_T grows and the tumour may eventually grow out of the saturated regime but by then treatment has already failed.

Both effects — the strong receptor density dependence and the weak injected amount dependence — are thus manifestations of the broader role of tumour size in determining outcome.

4.3 Hypoxia and reoxygenation

In the model, RL is distributed uniformly across the extracellular compartment regardless of vascular status, whereas oxygen is supplied by open capillaries and diffuses through tissue, creating hypoxic regions where vessels have been occluded. Hypoxic cells therefore receive the same RL exposure as normoxic cells. Thus the only mechanism by which hypoxia affects treatment outcome is through reduced radiosensitivity (α and β values).

In the model, hypoxic radioresistance is overcome by reoxygenation: as normoxic cells on the outer shell of the tumour are rendered apoptotic and eventually removed, local oxygen consumption drops, providing nearby hypoxic cells with an improved oxygen supply, restoring radiosensitivity and accelerating cell division, thereby speeding up induction of apoptosis in these cells. For larger tumours with a substantial hypoxic core, this reoxygenation cycle repeats inward like a wave, consistent with the increasing elimination times seen at large tumour sizes in Fig. 6. The claim that reoxygenation rather than direct hypoxic cell killing drives elimination is supported by the fact that hypoxic cells divide infrequently (at most a probability of 0.05 per day), meaning opportunities for radiation damage to induce apoptosis are rare.

The gradual inward erosion observed in Fig. 5 reflects a combination of three possible processes. First, despite radioresistance, hypoxic cells may still sustain sufficient damage to undergo apoptosis at their next division attempt. Reoxygenation might simply be accelerating

the cell cycle on the periphery as oxygen becomes more available with the induction of apoptosis in the outermost (normoxic) cells. Interestingly, this reoxygenation occurs just by induction of apoptosis, and the associated drop in oxygen consumption, and does not even require removal of cells and the subsequent reopening of capillaries, as shown by our lengthened apoptosis-removal simulation. Second, cells sustaining insufficient damage to die as hypoxic cells may reoxygenate, making previously sublethal damage lethal, through the abrupt change in α and β as cells revert from hypoxic to normoxic — more on this in 4.4 below. Third, reoxygenating cells, now more radiosensitive, continue to accumulate damage from RL that remains in the system. The relative importance of the three processes depends on radiobiological parameters, cell state conversion timescales, and RL clearance rate. Disentangling their contributions would require targeted numerical experiments.

4.4 Model limitations

Two limitations impact the applicability of the model behaviour to real tumours. First, hypoxic resistance is implemented phenomenologically by a change in α and β when cell types change. In reality, hypoxic cells accumulate less biological damage per unit of physical dose because of reduced oxygen-dependent fixation of DNA damage, and that damage remains unchanged through changes in cell type. In other words, model cells accumulate damage identically but normoxic and hypoxic cells interpret that damage differently upon attempting to divide. Real normoxic and hypoxic cells accumulate damage differently but interpret damage the same way upon attempting division. This means that the second process described above is not relevant in real tumours. This shortcoming would be fixed by a damage model that tracks damage and repair, with different repair rates in different cell types, and uses a single set of survival fraction parameters (α and β) in place of the LQ model with Lea-Catcheside G-factor.

Second, in real tumours, occluded capillaries reduce RL delivery to hypoxic regions just as they reduce oxygen delivery, raising the question of whether hypoxic resistance in RPT is primarily a radiobiological or a delivery effect. This makes the model's size dependence prediction unreliable for larger tumours with occluded vessels. In the model, vessel occlusion begins to appear once tumours reach about 400–450 cells ($\sim 120\mu$m radius) so our results regarding treatment failure below the size threshold are not influenced by this model limitation. Birindelli et al. [25] demonstrated computationally that in poorly vascularized tumour regions, only a small fraction of radiobiologically hypoxic tissue receives a therapeutic dose of ^{177}Lu-PSMA-617, implicating delivery failure as the dominant resistance mechanism in that setting. Since hypoxia and capillary occlusion are spatially correlated, disentangling these experimentally is difficult. A spatially resolved PK submodel, in which RL arrives via open capillaries and diffuses through the interstitium, would address this limitation directly. By separating the radiobiological and delivery effects, the present RL model isolates the radiobiological component and shows that hypoxia-induced radioresistance alone is insufficient to cause treatment failure — a result consistent with, and complementary to, the delivery-focused findings of Birindelli et al.

4.5 Multi-injection treatment protocols

Multi-injection RPT protocols are often motivated by the idea that a second injection timed to coincide with reoxygenation of hypoxic cells could exploit restored radiosensitivity to improve outcomes. In the present model, reoxygenation already plays a role within a single injection — the protracted delivery over several RL half-lives allows successive cycles of hypoxic reoxygenation. In this context, waiting longer between injections is beneficial simply because the tumour grows larger and the energy deposition fraction and total receptor content increase. There is no optimal interval, only a monotone transition from failure at short intervals to success at longer ones (Fig. 9). An optimal inter-injection interval would likely emerge in a model where RL delivery is spatially resolved and sensitive to vessel occlusion, such that a second injection timed too late would find the tumour's hypoxic core inaccessible to RL. This represents a further motivation for extending the model to include spatial PK.

4.6 Implications for treatment planning

The results presented here suggest several principles relevant to RPT treatment planning. First, the model predicts that single-injection RPT will fail for tumours below a threshold size at the time of treatment. Rather than waiting for tumours to grow — which risks the formation of new micrometastases in the interim — a more practical strategy would be a two-injection protocol: an initial injection to eliminate all suprathreshold tumours and cut off the source of new micrometastases, followed by a second injection timed to catch previously subthreshold tumours once they have grown above the threshold. The optimal inter-injection interval would be approximately the time required for a single-cell tumour to reach the threshold size. In principle, this could be estimated from tumour growth rate measurements and calibration of the actual size threshold. This provides a mechanistic basis for multi-injection RPT protocols that is distinct from the reoxygenation rationale often cited in traditional radiotherapy.

A second prediction of the model is that receptor density is a more productive target for improving treatment than escalating the injected amount, since receptors appear to be near saturation at clinically relevant injected amounts. Patient stratification by receptor expression — already practised in theranostics — is directly consistent with this finding.

Finally, capillary density affects the speed of treatment response, suggesting that patients with lower vascular density may require a longer observation window before response can be assessed rather than treatment escalation.

Our conclusions drawn from simulations involving only smaller tumours — ones below the threshold where vessel occlusion becomes significant — are robust. Those relating to larger tumours — particularly those in which occluded vessels ought to be restricting RL delivery — should be interpreted with that caveat in mind.

5 Appendix

5.1 Pharmacokinetics

The pharmacokinetics of the model are handled using a well-mixed compartment model consisting of ten ODEs for the total amount of hot and cold radioligand (RL) found in each of the compartments: central vascular (cen), tumour capillary (cap), tumour extracellular (ec), bound to tumour cells (b), and intracellular (ic). Our justification for the well-mixed assumption is based on the fact the typical distance traveled by the emitted beta particles is not small compared to the diameter of the tumours considered. Thus, in a spatial model, any spatial inhomogeneity in the RL distribution would get convolved with a broad kernel to get the distribution of radiation delivery. This smoothing suggests that it is not critical to model the spatial distribution of RL.

The reduced system used in the simulations is described in the main text. Here we present the full system and derive the reduced system from it. The full system is:

$$
\begin{aligned}
\frac{dN^x_{\text{cen}}}{dt} &= -\lambda_{\text{bio}} N^x_{\text{cen}} - F_T \left(\frac{N^x_{\text{cen}}}{V_{\text{cen}}} - \frac{N^x_{\text{cap}}}{V_{\text{v}}} \right) + (-1)^{n_x} \lambda_{\text{decay}} N^H_{\text{cen}}, \\
\frac{dN^x_{\text{cap}}}{dt} &= F_T \left(\frac{N^x_{\text{cen}}}{V_{\text{cen}}} - \frac{N^x_{\text{cap}}}{V_{\text{v}}} \right) + PS \left(\frac{N^x_{\text{ec}}}{V_{\text{ec}}} - \frac{N^x_{\text{cap}}}{V_{\text{v}}} \right) + (-1)^{n_x} \lambda_{\text{decay}} N^H_{\text{cap}} \\
\frac{dN^x_{\text{ec}}}{dt} &= -PS \left(\frac{N^x_{\text{ec}}}{V_{\text{ec}}} - \frac{N^x_{\text{cap}}}{V_{\text{v}}} \right) - \frac{k_{on} N^x_{\text{ec}}}{V_{\text{ec}}} \left(R_T - N_{\text{b}} \right) + k_{off} N^x_{\text{b}} + (-1)^{n_x} \lambda_{\text{decay}} N^H_{\text{ec}} \\
\frac{dN^x_{\text{b}}}{dt} &= \frac{k_{on} N^x_{\text{ec}}}{V_{\text{ec}}} \left(R_T - N_{\text{b}} \right) - k_{off} N^x_{\text{b}} - k_{int} N^x_{\text{b}} + (-1)^{n_x} \lambda_{\text{decay}} N^H_{\text{b}} \\
\frac{dN^x_{\text{ic}}}{dt} &= k_{int} N^x_{\text{b}} - k_{rel} N^x_{\text{ic}} + (-1)^{n_x} \lambda_{\text{decay}} N^H_{\text{ic}}
\end{aligned}
$$

where $x = H$ for hot/radioactive RL, $x = C$ for cold/decayed RL, $n_H = 1$, $n_C = 2$, and $N_{\text{b}} = N^H_{\text{b}} + N^C_{\text{b}}$ (the total number of bound receptors). The additional parameters not given in Table 2 are given in Table 4.

Nondimensionalizing this system, we use $1/\lambda_{bio}$ for the time scale and the typical injected amount of RL, N_0, as the scale for all the dependent variables. Using the substitution $M_{sub} = N_{sub}/N_0$ for all the variables, where *sub* is a placeholder for any of the subscripts, we get

Parameter	**Symbol**	**Value**	**Units**
Flow rate between the capillary and central compartments	F_T	2.9×10^{-3}	ℓ min^{-1}
Permeability rate between capillary and extracellular compartments	PS	3.5×10^{-3}	ℓ min^{-1}

Table 4: Definitions and values for the additional parameters required for the full PK model.

$$
\begin{aligned}
\frac{dM^x_{\text{cen}}}{dt} &= -M^x_{\text{cen}} - F\left(r_{vcen}M^x_{\text{cen}} - M^x_{\text{cap}}\right) + (-1)^{n_x}\lambda M^H_{\text{cen}},\\
\frac{dM^x_{\text{cap}}}{dt} &= F\left(r_{vcen}M^x_{\text{cen}} - M^x_{\text{cap}}\right) + P\left(r_{vec}M^x_{\text{ec}} - M^x_{\text{cap}}\right) + (-1)^{n_x}\lambda M^H_{\text{cap}}\\
\frac{dM^x_{\text{ec}}}{dt} &= -P\left(r_{vec}M^x_{\text{ec}} - M^x_{\text{cap}}\right) - K_{on}M^x_{\text{ec}}\left(R - M_{\text{b}}\right) + K_{off}M^x_{\text{b}} + (-1)^{n_x}\lambda M^H_{\text{ec}}\\
\frac{dM^x_{\text{b}}}{dt} &= K_{on}M^x_{\text{ec}}\left(R - M_{\text{b}}\right)) - K_{off}M^x_{\text{b}} - K_{int}M^x_{\text{b}} + (-1)^{n_x}\lambda M^H_{\text{b}}\\
\frac{M^x_{\text{ic}}}{dt} &= K_{int}M^x_{\text{b}} - K_{rel}M^x_{\text{ic}} + (-1)^{n_x}\lambda M^H_{\text{ic}}
\end{aligned}
$$

where $F = F_T/(\lambda_{bio}V_{\text{cap}})$, $r_{vcen} = V_{\text{cap}}/V_{cen}$, $\lambda = \lambda_{decay}/\lambda_{bio}$, $P = PS/\lambda_{bio}V_{\text{cap}}$, $r_{vec} = V_{\text{cap}}/V_{ec}$, $K_{on} = k_{on}M_0/(\lambda_{bio}V_{ec})$, $R = R_T/M_0$, $K_{off} = k_{off}/\lambda_{bio}$, $K_{int} = k_{int}/\lambda_{bio}$, and $K_{rel} = k_{rel}/\lambda_{bio}$. Estimating these nondimensional values, we find $F \approx 10^8$, $r_{vcen} \approx 10^{-7}$, $\lambda \approx 10^{-2}$, $P \approx 10^8$, $r_{vec} \approx 0.3$, $K_{on} \approx 10^{11}$, $R \approx 10^{-6}$, $K_{off} \approx 10^2$, $K_{int} \approx 10$, and $K_{rel} \approx 1$. We can see that the M_{cap}, M_{ec}, and M_b equations are fast and the M_{cen} and M_{ic} equations are slow. The QSS system is

$$
\frac{dM^x_{\text{cen}}}{dt} = -M^x_{\text{cen}} - F\left(r_{vcen}M^x_{\text{cen}} - M^x_{\text{cap}}\right) + (-1)^{n_x}\lambda M^H_{\text{cen}}, \tag{9}
$$

$$
0 = F\left(r_{vcen}M^x_{\text{cen}} - M^x_{\text{cap}}\right) + P\left(r_{vec}M^x_{\text{ec}} - M^x_{\text{cap}}\right) + (-1)^{n_x}\lambda M^H_{\text{cap}} \tag{10}
$$

$$
0 = -P\left(r_{vec}M^x_{\text{ec}} - M^x_{\text{cap}}\right) - K_{on}M^x_{\text{ec}}\left(R - M_{\text{b}}\right) + K_{off}M^x_{\text{b}} + (-1)^{n_x}\lambda M^H_{\text{ec}} \tag{11}
$$

$$
0 = K_{on}M^x_{\text{ec}}\left(R - M_{\text{b}}\right) - K_{off}M^x_{\text{b}} - K_{int}M^x_{\text{b}} + (-1)^{n_x}\lambda M^H_{\text{b}} \tag{12}
$$

$$
\frac{M^x_{\text{ic}}}{dt} = K_{int}M^x_{\text{b}} - K_{rel}M^x_{\text{ic}} + (-1)^{n_x}\lambda M^H_{\text{ic}} \tag{13}
$$

Examining the coefficients reveals that λ is at least three orders of magnitude smaller than any other coefficient in the QSS equations so we drop all the radioactive decay terms from equations (10), (11), (12). We find from the nondimensional M_{cap} equation, (10), that

$$
M^x_{\text{cap}} = \frac{r_{vcen}FM^x_{cen} + r_{vec}PM^x_{ec}}{F + P}.
$$

By combining equations (11) and (12), we find that

$$
M^x_{\text{cap}} = r_{vec}M^x_{ec} + \frac{K_{int}}{P}M^x_b. \tag{14}
$$

Equating these allows us to eliminate M^x_{cap}, getting

$$
M^x_{ec} = \frac{V_{ec}}{V_{cen}}M^x_{cen} - \frac{(F+P)K_{int}}{FPr_{vec}}M^x_b.
$$

We can rewrite this equation slightly to make better sense of it:

$$
\frac{M^x_{ec}}{V_{ec}} + \frac{(F+P)K_{int}}{FPr_{vec}}\frac{M^x_b}{V_{ec}} = \frac{M^x_{cen}}{V_{cen}}. \tag{15}
$$

This "concentration equation" says the central concentration is equal to the sum of the extracellular and bound concentrations, with a scale factor in front of the bound concentration. The scale factor in front of M_b^x/V_{ec} is of order 10^{-7} which suggests that the concentration in the extracellular compartment is essentially the same as in the central vascular compartment.

From Eq. (12), we get a system of equations for M_{b}^H and M_{b}^C in terms of M_{ec}^H and M_{ec}^C:

$$\begin{pmatrix} K_{on}M_{\mathrm{ec}}^H + K_{off} + K_{int} & K_{on}M_{\mathrm{ec}}^H \\ K_{on}M_{\mathrm{ec}}^C & K_{on}M_{\mathrm{ec}}^C + K_{off} + K_{int} \end{pmatrix} \begin{pmatrix} M_{\mathrm{b}}^H \\ M_{\mathrm{b}}^C \end{pmatrix} = \begin{pmatrix} K_{on}M_{\mathrm{ec}}^H R \\ K_{on}M_{\mathrm{ec}}^C R \end{pmatrix},$$

the solution to which is

$$M_{\mathrm{b}}^x = R \cdot \frac{M_{\mathrm{ec}}^x}{M_{\mathrm{ec}} + \kappa_\mu}$$

for $x \in \{H, C\}$ where $M_{\mathrm{ec}} = M_{\mathrm{ec}}^H + M_{\mathrm{ec}}^C$ and $\kappa_\mu = (K_{off} + K_{int})/K_{on}$. Plugging this into Eq. (15) gives us

$$\frac{M_{ec}^x}{V_{ec}} \left(1 + \frac{(F+P)K_{\mathrm{int}}}{FPr_{vec}} \frac{R}{M_{\mathrm{ec}} + \kappa_\mu}\right) = \frac{M_{cen}^x}{V_{cen}}.$$

The factor in parentheses is variable because of M_{ec} but M_{ec} is at most 1 and $\kappa_\mu \approx 10^{-9}$ so the entire factor is bounded between $1+10^{-12}$ and $1+10^{-3}$. We conclude that $M_{\mathrm{ec}}^x \approx V_{\mathrm{ec}} M_{\mathrm{cen}}^x / V_{\mathrm{cen}}$. Returning to Eq. (14) and substituting our expression for M_b^x, we get

$$M_{\mathrm{cap}}^x = \left(r_{vec} + \frac{K_{int}}{P} \frac{R}{M_{\mathrm{ec}} + \kappa_\mu}\right) M_{ec}^x.$$

In this expression, $r_{\mathrm{vec}} = 0.3$ and the second term in the parentheses is bounded between 10^{-13} and 10^{-4}. We conclude that $M_{\mathrm{cap}}^x \approx r_{\mathrm{vec}} M_{\mathrm{ec}}^x \approx V_{\mathrm{cap}} M_{\mathrm{cen}}^x / V_{\mathrm{cen}}$. In other words, the tumour vasculature and extracellular space rapidly equilibrate to the same concentration of radioligand as the central vascular compartment. Returning to the M_{b}^x expression above,

$$M_{\mathrm{b}}^x \approx R \frac{M_{\mathrm{ec}}^x}{M_{\mathrm{ec}} + \kappa_\mu} = R \frac{M_{\mathrm{cen}}^x}{M_{\mathrm{cen}} + V_{\mathrm{cen}} \kappa_\mu / V_{\mathrm{ec}}}.$$

Going back to the ODEs, we can simplify them to

$$\frac{dM_{\mathrm{cen}}^x}{dt} = -M_{\mathrm{cen}}^x - K_{int} M_{\mathrm{b}}^x + (-1)^{n_x} \lambda M_{\mathrm{cen}}^H, \tag{16}$$

$$\frac{dM_{\mathrm{ic}}^x}{dt} = K_{int} M_{\mathrm{b}}^x - K_{rel} M_{\mathrm{ic}}^x + (-1)^{n_x} \lambda M_{\mathrm{ic}}^H \tag{17}$$

where the $K_{int} M_{\mathrm{b}}^x$ term in the M_{cen}^x equation comes from chasing the F term through the QSS equations.

In dimensional form, the QSS system is

$$N_{\mathrm{b}}^x \approx R_T \frac{N_{\mathrm{cen}}^x}{N_{\mathrm{cen}} + V_{\mathrm{cen}}(k_{off} + k_{int})/k_{on}}.$$

$$N_{\mathrm{v}}^x \approx V_{\mathrm{cap}} N_{\mathrm{cen}}^x / V_{\mathrm{cen}}$$

$$N_{\mathrm{ec}}^x \approx V_{\mathrm{ec}} N_{\mathrm{cen}}^x / V_{\mathrm{cen}}$$

and

$$\frac{dN^x_{\text{cen}}}{dt} = -\lambda_{bio} N^x_{\text{cen}} - k_{int} N^x_{\text{b}} + (-1)^{n_x} \lambda_{decay} N^H_{\text{cen}}, \tag{18}$$

$$\frac{dN^x_{\text{ic}}}{dt} = k_{int} N^x_{\text{b}} - k_{rel} N^x_{\text{ic}} + (-1)^{n_x} \lambda_{decay} N^H_{\text{ic}} \tag{19}$$

where the $k_{int} N^x_{\text{b}}$ term in the N^x_{cen} equation comes from chasing the F_T term through the QSS equations. The $k_{int} N^x_{\text{b}}$ term in the N^x_{cen} equation is generally much smaller than the $\lambda_{bio} N^x_{\text{cen}}$ term and could have been left out of this equation but it illustrates the conservation between N^x_{cen} and N^x_{ic}. Omitting it allows the N_{cen} equations be solved independently (exponential decay), reducing the system to twos equation for N^x_{ic}.

Notice that N^x_b is in the form of number of receptors multiplied by a Michaelis-Menten function with the saturation based on both hot and cold radioligands. This is a mathematical manifestation of the idea that cold ligands act as a competitive ligand to the hot ones.

5.2 Comparison of PK models

The PK submodel initially consisted of a system of 10 ODEs tracking the hot and cold RLs across five compartment. The time scales varied from milliseconds through to days generating significant numerical limitations and motivating the use of multiple time scale methods (quasi-steady state, QSS, analysis). To test that our java implementation of the PK submodel was accurate, we compared it against a separate implementation in python as well as the full 10 variable PK submodel (using a stiff solver). This confirmed the accuracy of the QSS approximation and its implementation within the full model (see Fig. 11).

5.3 Intratumoural energy deposition fraction

The decision to treat the PK submodel as a well-mixed set of compartments has the benefit of not solving a multi-variable PDE but some useful information is lost. Using a PDE version of the model, finding the deposition of energy from the decaying RL throughout the tumour would require convolving the RL distribution with a kernel that encodes the average redistribution of energy from emission to deposition. For beta particles, this kernel would be a function that decays with distances and has an average redistribution distance of about 0.25 mm. Without the spatial information, the crudest approximation would be to assume that all the energy emitted gets deposited uniformly throughout the tumour. This could miss a lot of detail, especially for a tumour with a complex geometry. We implement a simple correction to recover at least one feature of the ideal calculation. The uniform assumption does not account for the fact that some of the emitted energy will land outside the tumour. For a small tumour, this can be dramatic. An extreme example is a tumour consisting of a single cell — a huge portion of the emitted energy would get spread to the surrounding healthy tissue.

To account for this loss of energy, we used the unpublished results of colleagues [56] which were obtained by Monte Carlo simulation of beta particle decay from within a tumour. From these simulations, we obtained a dose point kernel (DPK) which characterizes the redistribution of energy from emission to deposition and from that an intratumoural energy

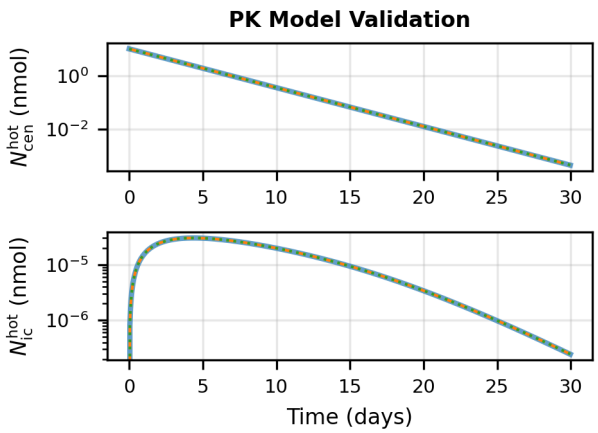

Figure 11: Comparison of three versions of the PK submodel: the full Java simulation with tumour dynamics frozen showing PK dynamics as implemented using the reduced QSS system (blue solid), the full PK submodel integrating all five compartments without the QSS assumption (green dotted), and the reduced PK submodel integrating only the central vascular and intracellular compartments with the others calculated using the QSS (orange dashed). Plots of both central vascular and intracellular compartments. The three solutions are indistinguishable by eye. The full PK system required use of a stiff solver (Python's BDF implementation of a backward-differentiation solver) for precisely the reason the QSS works (multiple time scales).

deposition fraction (EDF). The full Monte Carlo simulations and results will be described elsewhere. Here, we illustrate the idea using an abstract formulation that assumes the DPK takes a simple form that allows exact calculations.

We model the dose from Lu-177 beta particles emitted within the tumour back onto the tumour itself using a simplified geometric approach. Our model makes the simplifying assumption that each radioactive decay in the tumour emits a beta particle that, on average, deposits its energy uniformly within a sphere of radius ℓ (roughly twice the mean distance travelled) around the emission point, and that the tumour is spherical with radius R containing uniformly distributed radioactivity. Although for other reasons, our 3D extension of the tumour was cylindrical, its axial diameter is $2r_{\text{eff}}$ so a sphere captures the same basic scaling. Consider a tumour containing N_{hot} atoms of Lu-177 uniformly distributed throughout volume $V_{\text{tumour}} = \frac{4\pi}{3}R^3$. The volumetric activity density is $A(\vec{x}) = \lambda_{\text{decay}} N_{\text{hot}}/V_{\text{tumour}}$, where λ_{decay} is the Lu-177 decay constant. Each decay at position $\vec{x}$ deposits energy uniformly over a sphere of radius ℓ centered at $\vec{x}$, with volume $V_\ell = \frac{4\pi}{3}\ell^3$. The rate at which energy is deposited at a target point $\vec{y}$ from a source at $\vec{x}$ is therefore $A(\vec{x})\, dV/V_\ell$ when $|\vec{y} - \vec{x}| \leq \ell$, and zero otherwise.

The total rate of energy deposition at point $\vec{y}$ arises from all source points $\vec{x}$ within the tumour that lie within distance ℓ of $\vec{y}$. Since $A(\vec{x})$ is spatially uniform, this can be expressed as

$$\text{Dose rate at } \vec{y} = \frac{\lambda_{\text{decay}} N_{\text{hot}}}{V_{\text{tumour}} \cdot V_\ell} \cdot V_{\text{int}}(\vec{y}), \tag{20}$$

where $V_{\text{int}}(\vec{y})$ is the volume of intersection between the tumour sphere (radius R, centered at

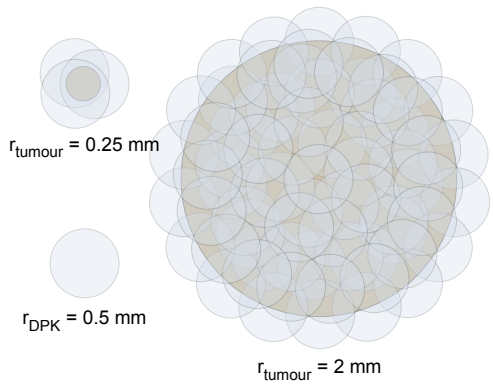

Figure 12: Illustration of the radius dependence of the Energy Deposition Fraction (EDF). Two tumours are shown (light brown), one with radius 0.25 mm and the other with radius 2 mm. The Dose Point Kernels (DPK) for the RLs are shown in translucent blue, representing our simplified DPK with a uniform deposition of beta particles across a circle of radius 0.5 mm. The larger tumour has more RL distributed across a larger area suggesting that cells within both tumours would receive the same dose. In fact, with the finite cutoff in this DPK, more than 0.5 mm away from the edge of the tumour, all cells do receive the same dose. Close to edge, some particles leave the tumour. For the smaller tumour, all points within the tumour are within 0.5 mm of the edge, thus receiving a smaller dose than most of the cells in the larger tumour. The fraction of the beta particles or equivalently of the deposited energy that remains in the tumour is the EDF.

the origin) and the deposition sphere (radius ℓ, centered at $\vec{y}$).

To obtain the total energy deposition rate within the tumour, we integrate over all points $\vec{y}$ inside the tumour, giving $E_{\text{in}} = \epsilon \int_{\text{tumour}} [\lambda_{\text{decay}} N_{\text{hot}}/(V_{\text{tumour}} \cdot V_\ell)] \cdot V_{\text{int}}(\vec{y})\, dV$, where ϵ is the mean beta particle energy per decay. The total energy emission rate from all decays in the tumour is $E_{\text{total}} = \lambda_{\text{decay}} N_{\text{hot}} \cdot \epsilon$. The intratumoural energy deposition fraction, defined as the ratio of the total energy deposition rate in the tumour to the total energy emission rate, is therefore

$$f_{\text{deposit}} = \frac{E_{\text{in}}}{E_{\text{total}}} = \frac{1}{V_{\text{tumour}}} \int_{\text{tumour}} \frac{V_{\text{int}}(\vec{y})}{V_\ell}\, dV. \tag{21}$$

Exploiting the spherical symmetry of the problem, we note that $V_{\text{int}}(\vec{y})$ depends only on $r = |\vec{y}|$, the distance from the tumour center. Converting to spherical coordinates, we obtain

$$f_{\text{deposit}} = \frac{9}{4\pi R^3 \ell^3} \int_0^R V_{\text{int}}(r)\, r^2\, dr, \tag{22}$$

where the factor out front comes from the two volumes in the denominator and a 4π in the numerator from the spherical integration.

The intersection volume $V_{\text{int}}(r)$ between the tumour sphere and a deposition sphere whose center is at distance r from the tumour center depends on the geometric configuration. When the spheres do not overlap ($r \geq R + \ell$), we have $V_{\text{int}}(r) = 0$. When one sphere is completely contained within the other ($r \leq |R - \ell|$), the intersection volume equals the volume of the smaller sphere, $V_{\text{int}}(r) = \frac{4\pi}{3} \min(R, \ell)^3$. For the case of partial overlap ($|R - \ell| < r < R + \ell$),

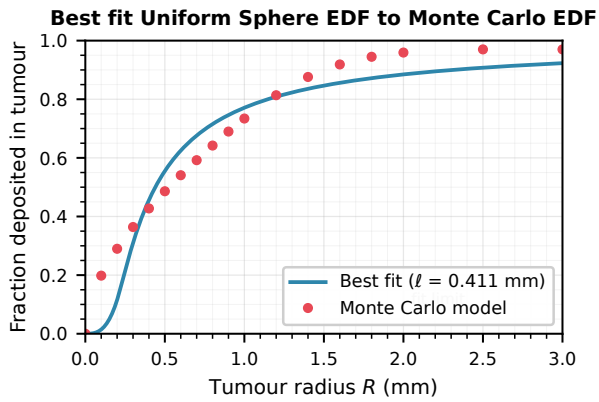

Figure 13: The EDF derived from the MC DPK (red dots) and the best fitting EDF derived from the Uniform Sphere DPK (blue) with optimal radius $\ell = 0.41$ mm. The fit is generally within an order of magnitude except near the origin (< 0.3 mm). This deviation suggests that using the best-fit uniform sphere model for the full simulation would be qualitatively similar but would differ quantitatively in the details.

the intersection volume is given by a standard formula for sphere-sphere intersection:

$$V_{\text{int}}(r) = \frac{\pi}{12r}(R + \ell - r)^2[r^2 + 2r(\ell + R) - 3(R - \ell)^2]. \tag{23}$$

We numerically calculated f_{deposit} using this expression for $V_{\text{int}}(r)$ and plotted it in Fig. 13 (blue curve).

For sufficiently small tumours ($R < \ell/2$), the tumour sphere is always completely contained within the deposition sphere of radius ℓ centered at any point within the tumour. In this regime, $V_{\text{int}}(r) = 4\pi R^3/3$ for all $r \in [0, R]$, and the integral simplifies to $f_{\text{deposit}} = R^3/\ell^3$. Thus in Fig. 13, the blue graph is exactly R^3/ℓ^3 between $R = 0$ and $R = \ell/2$.

Fig. 13 shows the EDF derived from the Uniform Sphere DPK model that best fits the EDF derived from the MC DPK model ($\ell = 0.41$ mm). The radius of the sphere can be thought of roughly as twice the mean beta path length. The MC DPK model results are shown as red dots. In the simulations, we use the MC DPK model results by interpolating values from a lookup table consisting of the coordinates of the red dots.

5.4 ODE formulation of the Lea-Catcheside G-factor

The Lea-Catcheside G-factor accounts for sub-lethal damage repair during protracted radiation exposure. Traditionally expressed in terms of nested integrals, it can be equivalently formulated as a system of ordinary differential equations (ODEs). This reformulation is mathematically identical but computationally more efficient, conceptually clearer, and more straightforward to generalize.

The survival fraction for protracted radiation delivery, as expressed by Lea and Catcheside, is:

$$SF = \exp(-\alpha D - \beta G D^2)$$

where the G-factor is:

$$G = \frac{2}{D^2} \int_0^T \dot{D}(t) \left[\int_0^t \dot{D}(t') e^{-\mu(t-t')} dt' \right] dt$$

where μ is the repair rate constant, T is the total irradiation time (h), $\dot{D}(t)$ is the dose rate at time t in Gy/h, and $D = \int_0^T \dot{D}(t)\, dt$ is the total dose in Gy.

The SF can also be expressed as

$$SF = \exp(-\alpha D - 2\beta G_{\text{alt}})$$

where the G_{alt}-factor is:

$$G_{\text{alt}} = \int_0^T \dot{D}(t) \left[\int_0^t \dot{D}(t') e^{-\mu(t-t')} dt' \right] dt.$$

While dividing and multiplying by D^2 makes the connection to the LQ model more explicit, this is a somewhat artificial means of illustrating the connection. Examining the integrals reveals the hidden squared dependence on the dose rate so the relationship is genuine but more subtle than a simple D^2 factor. Expressing it in the latter format avoids both artifice and an unnecessary division by D^2 which is impractical for the purpose of numerics when D is small or zero.

Simulating this by integrating the integrals is $O(n^2)$ so we reformulate it as an ODE. First, we define a function that tracks the amount of single-strand breaks in the DNA of a cell:

$$A(t) = \int_0^t \dot{D}(t') e^{-\mu(t-t')} dt'$$

and take its derivative:

$$\begin{aligned} \frac{dA}{dt} &= \dot{D}(t) \cdot e^0 + \int_0^t \dot{D}(t') \frac{\partial}{\partial t} \left[e^{-\mu(t-t')} \right] dt' \\ &= \dot{D}(t) - \mu \int_0^t \dot{D}(t') e^{-\mu(t-t')} dt' \\ &= \dot{D}(t) - \mu A(t). \end{aligned}$$

In words, single-strand breaks accumulate at a rate given by the incoming radiation $\dot{D}(t)$ and disappear with rate constant μ.

We define a second function that tracks the amount of double-strand breaks in a cell:

$$G_{\text{alt}} = \int_0^T \dot{D}(t) \cdot A(t)\, dt$$

which is the integral factor in G. For the ODE formulation, we take its derivative

$$\frac{dG_{\text{alt}}}{dt} = \dot{D}(t) \cdot A(t).$$

With this ODE formulation, we only need to keep track of the current state of DNA damage and exposure (D, A, G_{alt}). We do this for each age-cohort (all cells born on the same day) since each age cohort shares an exposure history and interpret these as population averages. When any particular cell attempts to divide, to determine if it survives or goes apoptotic from DNA damage, we use G_{alt} and D to calculate SF, as above, and check this probability against a random number ($U([0, 1])$).

Although we do not implement it in our current model, this ODE formulation opens the option of specifying different repair rates for different cells types (normoxic, hypoxic) or for different phases of the cell cycle, eliminating the need for different values of α and β in SF for normoxic and hypoxic cells.

5.5 Quasi-steady-state analysis of captive RL

We define captive RL as $N^H_{\text{captive}} = N^H_b + N^H_{\text{ic}}$, the hot-fraction RL directly associated with the tumour through binding or internalization. Starting from the QSS expression for the bound compartment (Eq. (3)),

$$N^H_b = R_T \frac{N^H_{\text{cen}}}{N_{\text{cen}} + K_M}, \tag{24}$$

and assuming N^H_{ic} is also at quasi-steady state,

$$N^H_{\text{ic}} = \frac{k_{\text{int}}}{k_{\text{rel}} + \lambda_{\text{decay}}} N^H_b, \tag{25}$$

we obtain

$$N^H_{\text{captive}} = \left(\frac{k_{\text{int}}}{k_{\text{rel}} + \lambda_{\text{decay}}} + 1 \right) N^H_b. \tag{26}$$

The central vascular compartment decays approximately exponentially: $N^H_{\text{cen}} \approx 0.1\, A\, e^{-(\lambda_{\text{bio}} + \lambda_{\text{decay}})t}$ and $N_{\text{cen}} \approx A\, e^{-\lambda_{\text{bio}} t}$, where the $k_{\text{int}} N_b$ sink term is negligible since $N_b \ll N_{\text{cen}}$ during the peak period. Substituting gives Eq. (6).

At $t = 0$ this simplifies to

$$N^H_{\text{captive}}(0) = \left(\frac{k_{\text{int}}}{k_{\text{rel}} + \lambda_{\text{decay}}} + 1 \right) R_T \cdot \frac{0.1\, A}{A + K_M}, \tag{27}$$

a Hill function in A with half-maximum at $A = K_M$.

There are two sources of error in this approximation. First, the N^H_{ic} quasi-steady-state assumption ignores the fact that the N_{cen} and N_{ic} compartments change on the same time scale. Second, R_T is calculated as the product of R_C and the number of cells in the tumour. Although we have assumed nothing about R_T in this calculation, the fact that it changes in time, possibly growing, possibly shrinking, depending on the response to treatment, the saturation argument strictly applies only at $t = 0$ and becomes messier with changes in tumour size. As explained in the main text, appealing to the simulation data, using the argument here as a guide on what variables to examine, we confirm that this prediction is at least qualitatively correct.

5.6 Fitting the 50% cure boundary to the injected-amount–receptor-density sweep

Equation (8) defines a one-parameter family of curves in the (A, R_C) plane, parameterized by σ, along which the predicted cure rate is constant. To fit σ to the 50% cure-rate level curve of the simulation data in Fig. 7, we extract the empirical 50% cure boundary from each column of the heatmap and then perform a least-squares fit to the full collection.

For each value of injected amount A_i, the column of the heatmap gives cure rates at discrete receptor densities. We fit a logistic function

$$g(R_C) = \frac{1}{1 + e^{-\kappa(R_C - R_C^{(i)})}} \tag{28}$$

to these cure rates by nonlinear least squares, where $R_C^{(i)}$ is the receptor density at which the fitted logistic equals 0.5 and $\kappa > 0$ is the steepness parameter.

This yields a set of points $\{(A_i, R_C^{(i)})\}$ representing the empirical 50% boundary. We then fit σ by minimizing the sum of squared residuals, which has the closed-form solution

$$\sigma = \frac{\sum_i R_C^{(i)} \left(1 + K_M/A_i\right)}{\sum_i \left(1 + K_M/A_i\right)^2}. \tag{29}$$

With $K_M = 4.3$ nmol, $P_0 = 52$ cells, and $(k_{\text{int}}/(k_{\text{rel}} + \lambda_{\text{decay}}) + 1) = 4.69$, the fitted value is $\sigma = 5.24 \times 10^{-10}$ nmol/cell, corresponding to

$$N_{1/2} = 0.1 \cdot P_0 \cdot \sigma \cdot \left(\frac{k_{\text{int}}}{k_{\text{rel}} + \lambda_{\text{decay}}} + 1\right) = 1.28 \times 10^{-17} \text{ mol} = 1.28 \times 10^{-8} \text{ nmol}. \tag{30}$$

6 Acknowledgements

We acknowledge funding support by the IAEA Marie Sklodowska-Curie Fellowship Programme (MSCFP) scholarship, the BC Cancer Foundation, and the Canadian Institutes of Health Research (CIHR) Project Grant PJT-162216. We also acknowledge helpful discussions with Dr. TJ McColl.

7 Data and Code Availability Statement

The code for the model is publicly available on GitHub:
https://github.com/ecytryn/TumourRPTmodel

References

[1] George Sgouros, Lisa Bodei, Michael R McDevitt, and Jessie R Nedrow. Radiopharmaceutical therapy in cancer: clinical advances and challenges. *Nat. Rev. Drug Discov.*, 19(9):589–608, September 2020.

[2] Ashutosh Dash, Sudipta Chakraborty, Maroor Raghavan Ambikalmajan Pillai, and Furn F Russ Knapp, Jr. Peptide receptor radionuclide therapy: an overview. *Cancer Biother. Radiopharm.*, 30(2):47–71, March 2015.

[3] Aidan Healy, Elaine Ho, Phillip Kuo, and Katherine Zukotynski. A brief overview of targeted radionuclide therapy trials in 2022. *Front. Nucl. Med.*, 3:1169650, June 2023.

[4] Jonathan Strosberg, Ghassan El-Haddad, Edward Wolin, Andrew Hendifar, James Yao, Beth Chasen, Erik Mittra, Pamela L Kunz, Matthew H Kulke, Heather Jacene, et al. Phase 3 trial of 177lu-dotatate for midgut neuroendocrine tumors. *New England Journal of Medicine*, 376(2):125–135, 2017.

[5] Oliver Sartor, Johann De Bono, Kim N Chi, Karim Fizazi, Ken Herrmann, Kambiz Rahbar, Scott T Tagawa, Luke T Nordquist, Nitin Vaishampayan, Ghassan El-Haddad, et al. Lutetium-177–psma-617 for metastatic castration-resistant prostate cancer. *New England Journal of Medicine*, 385(12):1091–1103, 2021.

[6] Wolfgang P Fendler, Kambiz Rahbar, Ken Herrmann, Clemens Kratochwil, and Matthias Eiber. 177lu-psma radioligand therapy for prostate cancer. *Journal of Nuclear Medicine*, 58(8):1196–1200, 2017.

[7] Clemens Kratochwil, Frederik L Giesel, Margarita Stefanova, Martina Benesova, Markus Bronzel, Ali Afshar-Oromieh, Walter Mier, Matthias Eder, Klaus Kopka, and Uwe Haberkorn. Targeted alpha therapy of metastatic castration-resistant prostate cancer with 225ac-psma-617: dosimetry estimate and empiric dose finding. *Journal of nuclear medicine*, 58(10):1624–1631, 2017.

[8] Tahir Yusufaly, Emilie Roncali, Julia Brosch-Lenz, Carlos Uribe, Abhinav K Jha, Geoffrey Currie, Joyita Dutta, Georges El-Fakhri, Helena McMeekin, Neeta Pandit-Taskar, Jazmin Schwartz, Kuangyu Shi, Lidia Strigari, Habib Zaidi, Babak Saboury, and Arman Rahmim. Computational nuclear oncology toward precision radiopharmaceutical therapies: Current tools, techniques, and uncharted territories. *Journal of Nuclear Medicine*, 66(4):509–515, February 2025.

[9] Joe O'Donoghue, Pat Zanzonico, John Humm, and Adam Kesner. Dosimetry in radiopharmaceutical therapy. *Journal of Nuclear Medicine*, 63(10):1467–1474, 2022.

[10] J.J. Rosales, M.L. Domínguez, L. Sancho, E. Prieto, M. de Arcocha, I. Torres, A. Roteta, R. Ramos, and G. Quincoces. State of the art and future perspectives of new radionuclides in nuclear medicine. *Revista Española de Medicina Nuclear e Imagen Molecular (English Edition)*, 44(1):500082, 2025.

[11] Siju C George and E James Jebaseelan Samuel. Developments in 177Lu-based radiopharmaceutical therapy and dosimetry. *Front. Chem.*, 11:1218670, July 2023.

[12] Keamogetswe Ramonaheng, Milani Qebetu, Honest Ndlovu, Cecile Swanepoel, Liani Smith, Sipho Mdanda, Amanda Mdlophane, and Mike Sathekge. Activity quantification and dosimetry in radiopharmaceutical therapy with reference to 177Lutetium. *Front. Nucl. Med.*, 4:1355912, March 2024.

[13] Stephen A. Graves and Robert F. Hobbs. Dosimetry for Optimized, Personalized Radiopharmaceutical Therapy. *Seminars in Radiation Oncology*, 31(1):37–44, January 2021.

[14] Andrea Farolfi, Wolfgang Fendler, Amir Iravani, Uwe Haberkorn, Rodney Hicks, Ken Herrmann, Jochen Walz, and Stefano Fanti. Theranostics for advanced prostate cancer: Current indications and future developments. *Eur. Urol. Oncol.*, 2(2):152–162, March 2019.

[15] Chalermrat Kaewput and Sobhan Vinjamuri. Update of PSMA theranostics in prostate cancer: Current applications and future trends. *J. Clin. Med.*, 11(10):2738, May 2022.

[16] J Harvey Turner. An introduction to the clinical practice of theranostics in oncology. *The British journal of radiology*, 91(1091):20180440, 2018.

[17] Matteo Bauckneht, Chiara Ciccarese, Riccardo Laudicella, Claudia Mosillo, Francesca D'Amico, Annunziato Anghelone, Alessandro Strusi, Viria Beccia, Sergio Bracarda, Giuseppe Fornarini, et al. Theranostics revolution in prostate cancer: Basics, clinical applications, open issues and future perspectives. *Cancer Treatment Reviews*, 124:102698, 2024.

[18] B Ribba, T Alarcón, K Marron, P K Maini, and Z Agur. The use of hybrid cellular automaton models for improving cancer therapy. In *Lecture Notes in Computer Science*, Lecture notes in computer science, pages 444–453. Springer Berlin Heidelberg, Berlin, Heidelberg, 2004.

[19] Shiva Shahmoradi, Fereidoun Nowshiravan Rahatabad, and Keivan Maghooli. A stochastic cellular automata model of growth of avascular tumor with immune response and immunotherapy. *Inform. Med. Unlocked*, 12:81–87, January 2018.

[20] Fateme Pourhasanzade and S H Sabzpoushan. A cellular automata model of chemotherapy effects on tumour growth: targeting cancer and immune cells. *Math. Comput. Model. Dyn. Syst.*, 25(1):63–89, January 2019.

[21] Hailey S H Ahn, Yas Oloumi Yazdi, Brennan J Wadsworth, K Bennewith, Arman Rahmim, and I Klyuzhin. Relating macroscopic PET radiomics features to microscopic tumor phenotypes using a stochastic mathematical model of cellular metabolism and proliferation. *Cancers*, 16(12):2215, June 2024.

[22] Nusrat J Begum, Anne Thieme, Nina Eberhardt, Robert Tauber, Calogero D'Alessandria, Ambros J Beer, Gerhard Glatting, Matthias Eiber, and Peter Kletting. The effect of total tumor volume on the biologically effective dose to tumor and kidneys for 177lu-labeled psma peptides. *Journal of Nuclear Medicine*, 59(6):929–933, 2018.

[23] Nusrat J Begum, Gerhard Glatting, Hans-Jürgen Wester, Matthias Eiber, Ambros J Beer, and Peter Kletting. The effect of ligand amount, affinity and internalization on psma-targeted imaging and therapy: A simulation study using a pbpk model. *Scientific reports*, 9(1):20041, 2019.

[24] Nouran R R Zaid, Remco Bastiaannet, Rob Hobbs, and George Sgouros. Mathematic modeling of tumor growth during [177Lu]Lu-PSMA therapy: Insights into treatment optimization. *J. Nucl. Med.*, 66(1):84–90, January 2025.

[25] Gabriele Birindelli, Milos Drobnjakovic, Volker Morath, Katja Steiger, Calogero D'Alessandria, Eleni Gourni, Ali Afshar-Oromieh, Wolfgang Weber, Axel Rominger, Matthias Eiber, and Kuangyu Shi. Is hypoxia a factor influencing PSMA-Directed radioligand Therapy?-An in silico study on the role of chronic hypoxia in prostate cancer. *Cancers*, 13(14), July 2021.

[26] Anahita Piranfar, Mohammad Souri, Arman Rahmim, and Madjid Soltani. Localized radiotherapy of solid tumors using radiopharmaceutical loaded implantable system: insights from a mathematical model. *Front. Oncol.*, 14:1320371, February 2024.

[27] Russell Rockne, Ellsworth C Alvord, Jason K Rockhill, and Kristin R Swanson. A mathematical model for brain tumor response to radiation therapy. *Journal of mathematical biology*, 58:561–578, 2009.

[28] A Dawson and T Hillen. Derivation of the tumour control probability (tcp) from a cell cycle model. *Computational and Mathematical Methods in Medicine*, 7(2-3):121–141, 2006.

[29] SFC O'Rourke, Helen McAneney, and Thomas Hillen. Linear quadratic and tumour control probability modelling in external beam radiotherapy. *Journal of mathematical biology*, 58(4):799–817, 2009.

[30] Rafael R Bravo, Etienne Baratchart, Jeffrey West, Ryan O Schenck, Anna K Miller, Jill Gallaher, Chandler D Gatenbee, David Basanta, Mark Robertson-Tessi, and Alexander RA Anderson. Hybrid automata library: A flexible platform for hybrid modeling with real-time visualization. *PLoS computational biology*, 16(3):e1007635, 2020.

[31] Juan A Delgado-SanMartin, Jennifer I Hare, Alessandro PS de Moura, and James WT Yates. Oxygen-driven tumour growth model: a pathology-relevant mathematical approach. *PLOS Computational Biology*, 11(10):e1004550, 2015.

[32] Thomas K Goldstick, Vincent T Ciuryla, and Leon Zuckerman. Diffusion of oxygen in plasma and blood. In *Oxygen transport to tissue—ii*, pages 183–190. Springer, 1976.

[33] JDB MacDougall and M McCabe. Diffusion coefficient of oxygen through tissues. *Nature*, 215(5106):1173–1174, 1967.

[34] Esteban Ortiz-Prado, Jeff F Dunn, Jorge Vasconez, Diana Castillo, and Ginés Viscor. Partial pressure of oxygen in the human body: a general review. *American journal of blood research*, 9(1):1, 2019.

[35] Brett A Wagner, Sujatha Venkataraman, and Garry R Buettner. The rate of oxygen utilization by cells. *Free Radical Biology and Medicine*, 51(3):700–712, 2011.

[36] Timothy J Strovas, Sarah C McQuaide, Judy B Anderson, Vivek Nandakumar, Marina G Kalyuzhnaya, Lloyd W Burgess, Mark R Holl, Deirdre R Meldrum, and Mary E Lidstrom. Direct measurement of oxygen consumption rates from attached and unattached cells in a reversibly sealed, diffusionally isolated sample chamber. *Advances in bioscience and biotechnology (Print)*, 5(5):398, 2010.

[37] Ioanna Papandreou, Rob A Cairns, Lucrezia Fontana, Ai Lin Lim, and Nicholas C Denko. Hif-1 mediates adaptation to hypoxia by actively downregulating mitochondrial oxygen consumption. *Cell metabolism*, 3(3):187–197, 2006.

[38] Michael Höckel and Peter Vaupel. Tumor Hypoxia: Definitions and Current Clinical, Biologic, and Molecular Aspects. *JNCI: Journal of the National Cancer Institute*, 93(4):266–276, 02 2001.

[39] Karsten Kossert, Ole J Nähle, Oliver Ott, and Rainer Dersch. Activity determination and nuclear decay data of 177lu. *Applied Radiation and Isotopes*, 70(9):2215–2221, 2012.

[40] J Kurth, BJ Krause, SM Schwarzenböck, L Stegger, M Schäfers, and K Rahbar. External radiation exposure, excretion, and effective half-life in 177lu-psma-targeted therapies. *EJNMMI research*, 8(1):32, 2018.

[41] Ayman Abouzayed, Kamila Seitova, Fanny Lundmark, Vitalina Bodenko, Maryam Oroujeni, Vladimir Tolmachev, Ulrika Rosenström, and Anna Orlova. 177lu-labeled psma targeting therapeutic with optimized linker for treatment of disseminated prostate cancer; evaluation of biodistribution and dosimetry. *Frontiers in Oncology*, 13:1221103, 2023.

[42] Peter Kletting, Christiane Schuchardt, Harshad R Kulkarni, Mostafa Shahinfar, Aviral Singh, Gerhard Glatting, Richard P Baum, and Ambros J Beer. Investigating the effect of ligand amount and injected therapeutic activity: a simulation study for 177lu-labeled psma-targeting peptides. *PLoS One*, 11(9):e0162303, 2016.

[43] David L Buckley, Caleb Roberts, Geoff JM Parker, John P Logue, and Charles E Hutchinson. Prostate cancer: evaluation of vascular characteristics with dynamic contrast-enhanced t1-weighted mr imaging—initial experience. *Radiology*, 233(3):709–715, 2004.

[44] Peter M Smith-Jones, Shankar Vallabahajosula, Stanley J Goldsmith, Vincent Navarro, Catherine J Hunter, Diego Bastidas, and Neil H Bander. In vitro characterization of radiolabeled monoclonal antibodies specific for the extracellular domain of prostate-specific membrane antigen. *Cancer research*, 60(18):5237–5243, 2000.

[45] Taylor J. McColl, Nouran R. R. Zaid, Carlos F. Uribe, and Arman Rahmim. A unified multi-scale s-value framework enabling pharmacokinetic-pharmacodynamic model coupling in radiopharmaceutical therapy. In *Proceedings of the SNMMI Annual Meeting*, June 2026.

[46] DE Lea and DG Catcheside. The mechanism of the induction by radiation of chromosome aberrations in tradescantia. *Journal of genetics*, 44:216–245, 1942.

[47] D. J. Brenner, L. R. Hlatky, P. J. Hahnfeldt, Y. Huang, and R. K. Sachs. The Linear-Quadratic Model and Most Other Common Radiobiological Models Result in Similar Predictions of Time-Dose Relationships. *Radiation Research*, 150(1):83, July 1998.

[48] Jian Z Wang, M Guerrero, and X Allen Li. How low is the α/β ratio for prostate cancer? *International Journal of Radiation Oncology* Biology* Physics*, 55(1):194–203, 2003.

[49] Henk B Kal and Marion PR Van Gellekom. How low is the α/β ratio for prostate cancer? *International Journal of Radiation Oncology* Biology* Physics*, 57(4):1116–1121, 2003.

[50] JZ Wang, XA Li, and NA Mayr. Dose escalation to combat hypoxia in prostate cancer: a radiobiological study on clinical data. *The British journal of radiology*, 79(947):905–911, 2006.

[51] David J Carlson, Robert D Stewart, and Vladimir A Semenenko. Effects of oxygen on intrinsic radiation sensitivity: a test of the relationship between aerobic and hypoxic linear-quadratic (lq) model parameters a. *Medical physics*, 33(9):3105–3115, 2006.

[52] Yusuf Emre Erdi. Limits of tumor detectability in nuclear medicine and pet. *Molecular imaging and radionuclide therapy*, 21(1):23, 2012.

[53] Stephen Adler, Jurgen Seidel, Peter Choyke, Michael V Knopp, Katherine Binzel, Jun Zhang, Craig Barker, Shielah Conant, and Roberto Maass-Moreno. Minimum lesion detectability as a measure of pet system performance. *EJNMMI physics*, 4(1):13, 2017.

[54] Alan L Ho, Ravinder K Grewal, Rebecca Leboeuf, Eric J Sherman, David G Pfister, Desiree Deandreis, Keith S Pentlow, Pat B Zanzonico, Sofia Haque, Somali Gavane, et al. Selumetinib-enhanced radioiodine uptake in advanced thyroid cancer. *New England Journal of Medicine*, 368(7):623–632, 2013.

[55] Florian Rosar, Robert Neher, Caroline Burgard, Johannes Linxweiler, Mathias Schreckenberger, Manuela A Hoffmann, Mark Bartholomä, Fadi Khreish, and Samer Ezziddin. Upregulation of psma expression by enzalutamide in patients with advanced mcrpc. *Cancers*, 14(7):1696, 2022.

[56] Cassandra Miller, Ivan Klyuzhin, Guillaume Chaussé, Julia Brosch-Lenz, Helena Koniar, Kuangyu Shi, Arman Rahmim, and Carlos Uribe. Impact of cell geometry, cellular uptake region, and tumour morphology on 225ac and 177lu dose distributions in prostate cancer. *EJNMMI physics*, 11(1):97, 2024.